

Daily Drought Prediction in the Huaihe River Basin Using VMD-informer-LSTM

Min Li^{1,2}, Ming Ou¹, Yuhang Yao¹, Changman Yin¹

1 College of Hydraulic Science and Engineering, Yangzhou University, Yangzhou, China, 225000

[2 National Key Laboratory of Water Disaster Prevention, Hohai University, Nanjing, China,
210098](#)

Correspondence to: Min Li (limintju@126.com)

Abstract

Accurate drought prediction is a key challenge in water resource management and agricultural planning. This study proposes a novel drought prediction framework that integrates Variational Mode Decomposition (VMD), Informer, and Long Short-Term Memory (LSTM) networks to enhance hydrological drought forecasting in the Huaihe River Basin, China. The VMD-Informer-LSTM model decomposes complex non-stationary drought sequences into multi-scale components, effectively extracting long-term trends and short-term fluctuations. Results show that the model outperforms LSTM, Transformer-LSTM, and Informer-LSTM, improving R^2 , RMSE, MAE, and MAPE by 28.4%, 46.2%, 46.5%, and 50.8%, respectively, over the baseline LSTM. When the prediction period is 30 days, the VMD-Informer-LSTM achieves the highest prediction accuracy. During the 120–180 day prediction period, the prediction accuracy of all models declines, with drought intensity generally underestimated. Misclassifications are mainly concentrated in the transition zones between humid and semi-humid regions, with higher error frequency in semi-humid areas. Prediction accuracy is highest in the upstream and downstream regions, followed by the Yishuisi River Basin, while the midstream region performs poorly due to human interference. Shapley Additive Explanations (SHAP) further reveal that precipitation and temperature are the dominant meteorological drivers, jointly accounting for nearly half of the model's predictive power. These results confirm that the VMD-Informer-LSTM provides the most accurate predictions among the tested models, offering valuable support for drought risk assessment and water resource management in the Huaihe River Basin and other similar regions.

Keywords: Drought prediction, DEDI, Variational Mode Decomposition, informer, LSTM

1 Introduction

Drought represents one of the most spatially extensive, temporally persistent, and far-reaching natural disasters globally, with complex formation mechanisms involving intricate interactions between atmospheric circulation patterns, land surface processes, and human activities (Alsubih et al., 2021; Dai, 2013). Drought events not only directly threaten watershed water security and agricultural productivity but also profoundly affect regional ecosystem stability and socioeconomic development (Zhang et al., 2018). With intensifying climate change and increasing human activity intensity, drought events exhibit significant upward trends in frequency, intensity, and spatial extent (Cook et al., 2020; Trenberth et al., 2014). Therefore, accurate drought prediction is crucial for developing scientific disaster mitigation strategies, optimizing water resource allocation schemes,

39 and ensuring regional food and ecological security.

40 However, drought prediction faces major challenges due to the inherent complexity of drought
41 phenomena (Hao et al., 2017). Drought occurrence and evolution are controlled by multiple natural
42 and anthropogenic factors, including precipitation distribution, evapotranspiration processes,
43 topographic conditions, land use changes, and human interventions (AghaKouchak et al., 2015;
44 Vicente-Serrano et al., 2018). These factors generate highly complex, nonlinear, and non-stationary
45 spatiotemporal evolution patterns. Drought time series typically contain multi-scale periodic
46 oscillations, long-term trend changes, and stochastic fluctuation components that are mutually
47 coupled and interdependent, forming extremely complex dynamical systems (Belayneh et al., 2014;
48 Huang et al., 2015).

49 Traditional drought prediction methods rely on physics-based numerical models and st
50 atistical regression approaches (Dutra et al., 2014; Yuan & Quiring, 2017). Physics-based
51 methods include Global Climate Models (GCMs) such as the ECMWF and NCEP-CFSv2,
52 which can provide global-scale long-term climate predictions but have coarse spatial resolu
53 tions (typically 100-200 km) and cannot adequately capture regional drought characteristics
54 (Saha et al., 2014). Regional Climate Models (RCMs) employ dynamic downscaling techni
55 ques to achieve high resolutions (10-50 km) but inherit systematic biases from driving mo
56 dels and require substantial computational resources (Jacob et al., 2014; Rummukainen, 20
57 10). Land surface models such as Variable Infiltration Capacity (VIC), Community Land
58 Model (CLM), and Noah simulate coupled water cycle, energy balance, and vegetation dyn
59 amics processes but are highly sensitive to meteorological forcing data quality and paramet
60 erization schemes (Ek et al., 2003; Lawrence et al., 2011). Statistical methods include line
61 ar regression approaches, time series analysis and spectral/wavelet analysis techniques, etc
62 (Box et al., 2015; Modarres, 2007). Time series models, such as Autoregressive Moving A
63 verage (ARMA), Autoregressive Integrated Moving Average (ARIMA) models, Random Fo
64 rest (RF), demonstrate certain capabilities for stationary time series. However, their predicti
65 on performance significantly deteriorates on non-stationary, multi-periodic drought sequen
66 ces (Mishra & Desai, 2005; Mossad & Alazba, 2015). Despite contributions from these tradi
67 tional methods, fundamental limitations persist across both physics-based and statistical app
68 roaches (Hao et al., 2017; Morid et al., 2006). Rigid model structures in both GCMs and
69 RCMs cannot adaptively adjust to accommodate intrinsic data characteristics. Insufficient n
70 onlinear processing capabilities in land surface models and statistical methods (including A
71 RMA, ARIMA, and RF models) cannot capture complex feedback mechanisms and thresho
72 ld effects(AghaKouchak et al., 2015). Additionally, there are difficulties in multi-scale infor
73 mation integration and heterogeneous data fusion, particularly in land surface models and
74 GCMs (Wood et al., 2016). High parameter sensitivity affects the robustness and generaliz
75 ation capability of both physics-based and statistical models (including ARMA, ARIMA, a
76 nd RF models) (Svoboda et al., 2002). Finally, trade-offs between computational efficiency
77 and accuracy challenge the operational implementation requirements of RCMs and complex
78 statistical models (Mo, 2008; Yuan & Quiring, 2017).

79 Recent advances in artificial intelligence and big data technologies have fundamentally
80 transformed time series modeling and prediction across multiple fields (LeCun et al., 2015;
81 Shlezinger et al., 2023). Deep learning methods demonstrate significant advantages in automatically
82 capturing complex patterns and latent features without requiring pre-specified physical relationships,

83 possessing powerful nonlinear mapping and adaptive learning capabilities (Bengio et al., 2013;
84 Schmidhuber, 2015). Long-Short-Term Memory (LSTM) networks have been successfully applied
85 to various hydrological nonlinear sequence modeling tasks, including streamflow prediction, flood
86 forecasting, and water level estimation, demonstrating superior predictive performance (Kratzert et
87 al., 2018; Zhang et al., 2014). LSTM networks through their unique gate mechanisms and memory
88 cell design effectively address gradient vanishing problems in traditional recurrent neural networks
89 and exhibit excellent performance in capturing long-term dependency information (Greff et al.,
90 2017). However, single deep learning architectures still have limitations when processing complex
91 time series data, and multi-model ensemble and parallel architecture designs provide novel
92 approaches for further enhancing prediction performance (Mosavi et al., 2018; Sit et al., 2020).

93 To enhance model capability for processing non-stationary complex sequences, signal
94 decomposition algorithms for data preprocessing have become key strategies for improving time
95 series prediction performance. Variational Mode Decomposition (VMD), an advanced adaptive
96 signal decomposition technique proposed by Dragomiretskiy and Zosso in 2014, decomposes non-
97 linear, non-stationary complex sequences into multiple Intrinsic Mode Functions (IMFs) with
98 different center frequencies. Each IMF reflects the dynamic characteristics of the original sequence
99 at specific frequency levels, possessing relatively independent frequency bandwidth and amplitude
100 modulation properties (Dragomiretskiy & Zosso, 2014). Compared to traditional decomposition
101 methods such as Empirical Mode Decomposition (EMD) and Ensemble EMD (EEMD), VMD is
102 based on rigorous variational optimization theoretical frameworks, employs completely non-
103 recursive decomposition models, effectively avoids mode mixing and end-effect problems, and
104 possesses superior frequency separation effects and noise robustness.

105 In recent years, Transformer architectures have achieved major breakthroughs in time series
106 prediction, particularly the informer model specifically optimized for long time series prediction
107 tasks. Zhou proposed that informer reduces computational complexity from $O(L^2)$ to $O(L\log L)$
108 through Probabilistic Sparse Self-attention mechanisms, combined with self-attention distillation
109 operations that progressively compress sequence length layer by layer, significantly improving
110 efficiency and accuracy in processing lengthy sequences (Zhou et al., 2021a). This innovative
111 architecture provides novel technical pathways for capturing long-range temporal dependencies.

112 This study adopts the Daily Evapotranspiration Deficit Index (DEDI) as a drought monitoring
113 indicator, constructed based on daily actual and potential evapotranspiration from ERA5 reanalysis
114 data, which can effectively reflect the dynamic evolution processes of regional droughts (Hersbach
115 et al., 2020; Zhang et al., 2022; Zuo et al., 2020). Building upon this foundation, we propose a novel
116 drought prediction model integrating Variational Mode Decomposition, informer, and Long Short-
117 Term Memory networks (VMD-informer-LSTM), which is expected to provide a high-accuracy,
118 robust prediction framework for drought prediction applications by combining the technical
119 advantages of variational optimization decomposition, probabilistic sparse attention mechanisms,
120 and gated memory networks. Through a combination of multiscale feature decomposition and
121 hybrid deep learning architectures, this method effectively handles the non-stationary characteristics
122 of complex drought indices like DEDI, accurately capturing long-range climate trends and short-
123 term fluctuations. This study significantly improved prediction accuracy and reliability of complex
124 non-stationary drought time series and provided scientific foundations for regional water resource
125 management and drought risk assessment (Pozzi et al., 2013; Willmott & Matsuura, 2005).

126 The technical approach includes: (1) utilizing VMD for adaptive modal decomposition of

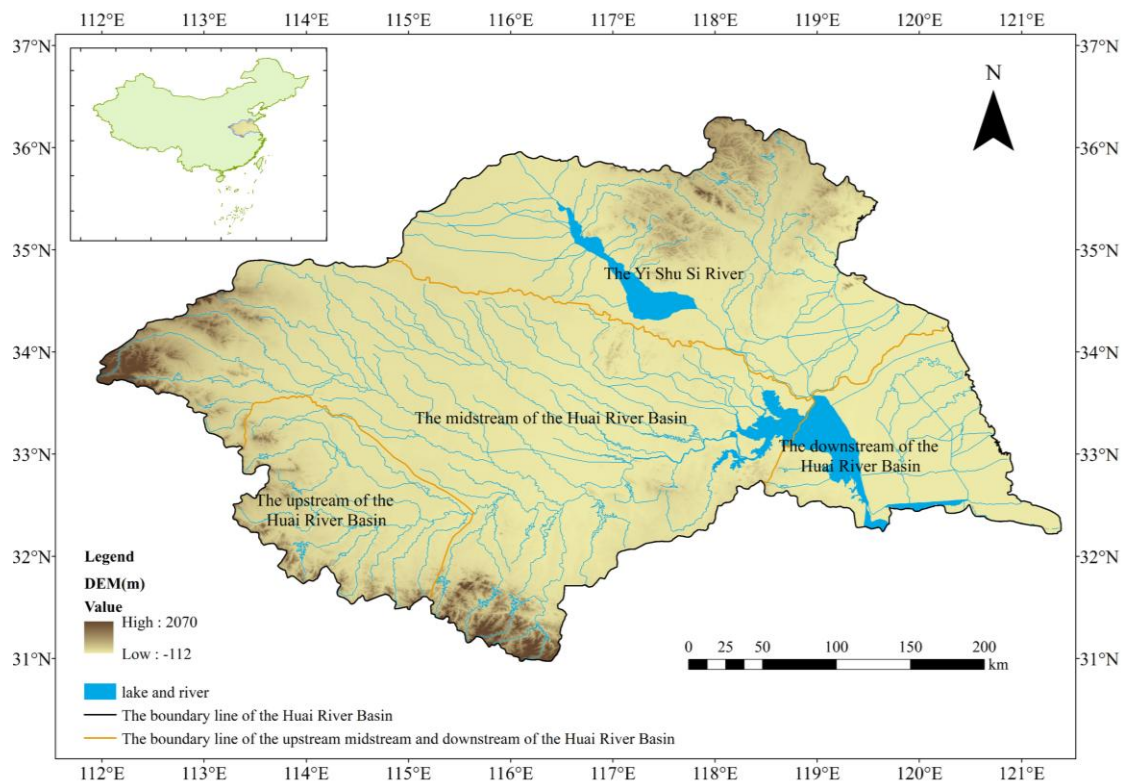
127 original DEDI sequences, deconstructing complex nonlinear time series into multi-frequency scale
128 IMF components to achieve structured extraction of multi-scale features (Dragomiretskiy & Zosso,
129 2014; Johny et al., 2022); (2) constructing dual-branch parallel architecture of informer and LSTM,
130 where informer efficiently captures global trends of long-range sequences through probabilistic
131 sparse attention mechanisms, while LSTM precisely models local temporal dynamics through
132 gating mechanisms (Zhou et al., 2021b); (3) fusing dual-source features through fully connected
133 layers to form hybrid feature representations possessing both long-range dependency analysis
134 capability and short-term fluctuation capture ability (Li et al., 2023; Zhang et al., 2019); (4) adopting
135 a three-stage design of decomposition-parallelization-fusion to obtain final drought prediction
136 results.

137 2 Study Area and data

138 2.1 Study Area

139 The Huaihe River Basin originates from the Tongbai Mountains in Nanyang City, Henan
140 Province, China. It is located between 111°55'-121°20'E longitude and 30°55'-36°20'N latitude,
141 covering approximately 270,000 km². The basin is situated in China's north-south climate transition
142 zone, with the area north of the Huaihe River belonging to the warm temperate zone and the area
143 south of the river belonging to the northern subtropical zone (Yao et al., 2024). The annual mean
144 temperature ranges from 11-16°C, with temperature variations increasing from north to south and
145 from coastal to inland areas. The Huaihe River Basin receives a multi-year average precipitation of
146 883 mm, with a spatial distribution characterized by higher precipitation in mountainous areas
147 compared to plains, increased precipitation along the coast than inland, and a decreasing gradient
148 from south to north. The multi-year average evaporation in the basin fluctuates between 650-1250
149 mm, primarily concentrated during May-August, with an overall decreasing trend from south to
150 north and from east to west. The studied region is shown in Fig. 1.

151 During the 62-year period from 1949 to 2010, the Huaihe River Basin experienced cumulative
152 drought-affected areas of 167 million hectares, with disaster-affected areas of 87.3 million hectares,
153 resulting in grain losses of 13.96 billion kg. On average, 2.698 million hectares of crops were
154 affected by drought annually, with 1.408 million hectares suffering disaster-level impacts (Gao et
155 al., 2015). Drought disasters have severely impacted industrial and agricultural production, urban
156 and rural water supply security, and ecological environments within the basin, becoming one of the
157 primary factors constraining rapid and sustainable socio-economic development in the region.
158 Therefore, providing reliable drought prediction methods is of great significance for accurate
159 drought forecasting and the scientific development of drought response strategies in the Huaihe
160 River Basin.



161
162

Figure 1 The study area of Huaihe river Basin

163 2.2 Data Sources

164 This study utilizes daily actual evapotranspiration, potential evapotranspiration, surface
 165 pressure, cloud cover, maximum temperature, mean temperature, wind speed, and precipitation data
 166 for the period 1980-2020, sourced from the fifth-generation high-resolution atmospheric reanalysis
 167 product (ECMWF Reanalysis v5, ERA5) developed by the European Centre for Medium-Range
 168 Weather Forecasts (ECMWF). ERA5 data are characterized by extensive coverage, long time series,
 169 and excellent spatio-temporal consistency. This makes them an optimal data choice for long-term
 170 and high-resolution analyses. To meet the specific spatial resolution requirements of this study, the
 171 downloaded ERA5 data were further subjected to interpolation processing. This converted them to
 172 a spatial resolution of $0.25^\circ \times 0.25^\circ$ to more precisely match the spatial characteristics of the study
 173 region (Muñoz-Sabater et al., 2021). Land use data for 2005, 2010, 2015, and 2020 with a spatial
 174 resolution of 1 km were obtained from the Data Center for Resources and Environmental Sciences,
 175 Chinese Academy of Sciences (<https://www.resdc.cn/>).

176 3. Methods

177 3.1 DEDI Index

178 The Daily Evapotranspiration Deficit Index (DEDI) is a daily drought index constructed based
 179 on daily evapotranspiration as well as potential evapotranspiration for monitoring and predicting
 180 regional drought events (Zhang et al., 2022). This index is calculated based on ERA5 data provided
 181 by ECMWF.

182 The DEDI is calculated as follows:

$$DEDI_i = \frac{D_i - D_{AVE}}{D_{STU}} \quad (1)$$

$$D_i = AET_i - PET_i \quad (2)$$

183 where i represents time, AET_i represents the actual evapotranspiration on day i (units:
 184 mm/day), PET_i represents the potential evapotranspiration on day i (units: mm/day), D_i
 185 represents the evapotranspiration deficit between AET and PET on day i , and D_{AVE} and D_{STU} are
 186 the multi-year climatological mean and standard deviation, respectively (Zuo et al., 2020).

187 3.2 VMD

188 Variational Mode Decomposition (VMD) was proposed by Konstantin Dragomiretskiy
 189 (Dragomiretskiy & Zosso, 2014) as a signal processing method designed to effectively overcome
 190 mode mixing and end effect problems existing in Empirical Mode Decomposition (EMD). Unlike
 191 the recursive decomposition principle of EMD, VMD determines the central frequency and
 192 bandwidth of each mode component. This is done by constructing and solving the optimal solution
 193 to a variational model. This represents a completely non-recursive decomposition model. This
 194 method searches for a set of mode components and their corresponding center frequencies through
 195 an iterative search. This ensures that each mode maintains smoothness after demodulation to
 196 baseband.

197 The adaptivity of VMD is reflected in its ability to automatically determine the number of
 198 modes decompositions according to signal characteristics and adaptably match the optimal center
 199 frequency and finite bandwidth for each mode, thereby achieving effective separation of Intrinsic
 200 Mode Functions (IMFs) and frequency domain partitioning of signals. Experimental results
 201 demonstrate that VMD exhibits strong robustness in sampling and noise aspects, is capable of
 202 reducing the non-stationarity of time series with high complexity and strong non-linearity and
 203 decomposing them into multiple sub-sequences with different frequency scales that are relatively
 204 stationary, making it particularly suitable for non-stationary signal processing.

205 VMD decomposes time series into simple high-frequency and low-frequency intrinsic mode
 206 functions through optimization processes, improving signal processing stability and accuracy. This
 207 method is not only theoretically innovative but also demonstrates superior performance in practical
 208 applications, providing an effective tool for non-stationary signal analysis. Research by Zhao et al.
 209 (2023) further proved VMD's excellent performance in handling boundary effects by adjusting
 210 parameters (such as decomposition levels, quadratic penalty terms, etc.) to effectively control
 211 deviations in decomposition results, thereby improving model adaptability (Zhang et al., 2023; Zhao
 212 et al., 2023).

213 In this study, two key parameters of the Variational Mode Decomposition (VMD) need to be
 214 predefined: the penalty factor α (bandwidth constraint parameter) and the number of modes K (i.e.,
 215 the number of intrinsic mode functions, IMFs). The penalty factor α is empirically determined based
 216 on the length of the time series, with its value ranging from 1.5 to 2.0 times the sample length,
 217 aiming to balance frequency band separation and decomposition stability. When α is relatively small,
 218 the bandwidth of each IMF becomes wider, which may lead to spectral overlap between different
 219 modes and thus reduce the physical interpretability of the decomposition results; whereas when α is
 220 excessively large, the bandwidth is overly constrained, making the decomposition more sensitive to
 221 noise. In this study, α is finally set to 1.75 times the sample length. In addition, the number of modes
 222 K is determined based on the frequency distribution characteristics of the decomposed signal and

223 [preliminary experimental results. When K is less than 7, certain IMF components exhibit significant](#)
 224 [spectral mixing, making it difficult to effectively separate signals at different time scales; when K](#)
 225 [exceeds 7, the center frequencies of adjacent IMFs become too close and the energy distribution](#)
 226 [tends to be dispersed, resulting in redundant or noise-dominated modes and thus reducing the](#)
 227 [stability and physical interpretability of the decomposition. Therefore, K is uniformly set to 7 in this](#)
 228 [study to ensure effective separation of the dominant frequency components of the original DEDI](#)
 229 [series while avoiding redundancy caused by over-decomposition. Preliminary experiments](#)
 230 [conducted on several representative grid points indicate that this parameter combination yields](#)
 231 [stable decomposition results and satisfactory predictive performance. To maintain methodological](#)
 232 [consistency and avoid potential spatial overfitting, the same VMD parameter settings are applied](#)
 233 [uniformly across all grid points in the study area.](#)

234 Assuming the original signal f is decomposed into k components, ensuring that the decomposed
 235 sequences are modal components with finite bandwidth and center frequencies, while minimizing
 236 the sum of estimated bandwidths of all modes, with the constraint that the sum of all modes equals
 237 the original signal, the VMD constrained variational model is as follows:

$$\min_{\{u_k, \omega_k\}} \left\{ \sum_{k=1}^K \left\| \partial_t \left[\left(\delta(t) + \frac{j}{\pi t} \right) * u_k(t) \right] e^{-j\omega_k t} \right\|_2^2 \right\} \quad (3)$$

$$\text{s. t. } \sum_k u_k = f(t) \quad (4)$$

$$u_k = \{u_1, u_2, \dots, u_k\} \quad (5)$$

$$\omega_k = \{\omega_1, \omega_2, \dots, \omega_k\} \quad (6)$$

238 where $f(t)$ represents the original data; K represents the number of modal components;
 239 $\delta(t)$ represents the Dirac function; $*$ represents convolution operation; ∂_t is the partial derivative
 240 operator; $\{u_k\}$ represents the k -th component function obtained through calculation; $\{\omega_k\}$
 241 represents the center frequency of the k -th component obtained through calculation.

242 The augmented LaGrange is introduced to solve this constrained optimization problem:

$$\begin{aligned} L(\{u_k\}, \{\omega_k\}, \lambda) = & \alpha \sum_k \left\| \partial_t \left[\left(\delta(t) + \frac{j}{\pi t} \right) * u_k(t) \right] e^{-j\omega_k t} \right\|_2^2 \\ & + \left\| f(t) - \sum_k u_k(t) \right\|_2^2 + \left\langle \lambda(t), f(t) - \sum_k u_k(t) \right\rangle \end{aligned} \quad (7)$$

243 where α represents the penalty factor; $\lambda(t)$ represents the Lagrange multiplier.

244 The alternating direction method of multipliers (ADMM) is used to find the saddle point of the
 245 augmented LaGrange. In the frequency domain, the updates are:

$$\hat{u}_k^{n+1}(\omega) = \frac{\hat{f}(\omega) - \sum_{i \neq k}^k \hat{u}_i^{n+1}(\omega) + \frac{\hat{\lambda}^n(\omega)}{2}}{1 + 2\alpha(\omega - \omega_k^n)^2} \quad (8)$$

$$\omega_k^{n+1} = \frac{\int_0^\infty \omega |u_k^{n+1}(\omega)| d\omega}{\int_0^\infty |u_k^{n+1}(\omega)| d\omega} \quad (9)$$

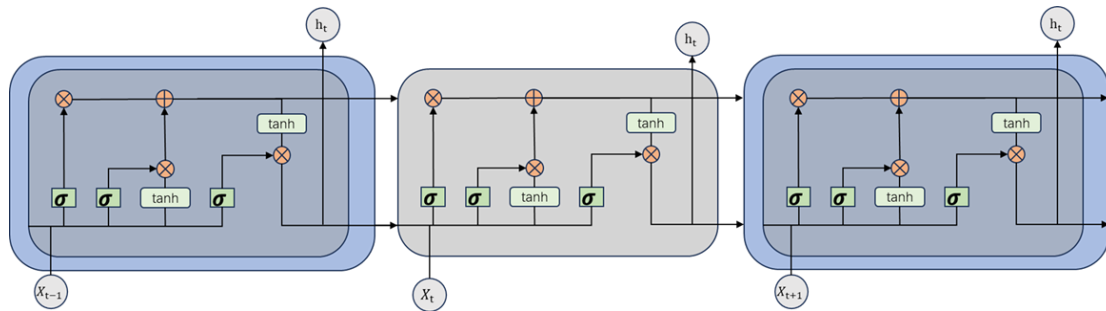
$$\hat{\lambda}^{n+1}(\omega) \leftarrow \hat{\lambda}^n(\omega) + \pi \left[\hat{f}(\omega) - \sum_{i \neq k} \hat{u}_i^{n+1}(\omega) \right] \quad (10)$$

246 where γ represents noise tolerance; the $\hat{u}_k^{n+1}(\omega)$ represent Wiener filtering residuals; $\hat{u}_i(\omega)$,
 247 and $\hat{\lambda}^n(\omega)$ represent the Fourier transforms of $u(t)$ and $\lambda(t)$, respectively.

248 3.3 LSTM

249 The Long-Short-Term Memory (LSTM) models are a special type of Recurrent Neural
 250 Network (RNN) variant that addresses the gradient vanishing problem in RNN processing of long
 251 sequence data by introducing memory cells (Cell States), specifically designed for processing time
 252 series data (Hochreiter & Schmidhuber, 1997). When recording long sequence data, RNN
 253 experiences gradient vanishing or exploding due to continuous information accumulation, making
 254 it difficult for the network to learn long-term dependencies, ultimately affecting the model's accurate
 255 capture of trends and periodicity in time series data (Jaseena & Kooor, 2022).

256 LSTM aims to solve the gradient-vanishing or exploding problems encountered by traditional
 257 RNN when processing long sequence data. This is done mainly through gate mechanisms regulating
 258 information flow. The LSTM model consists of four interacting layers: input gate, forget gate, cell
 259 state gate, and output gate. It is shown in Fig. 2 below.



260
261 Figure 2 The construction of LSTM

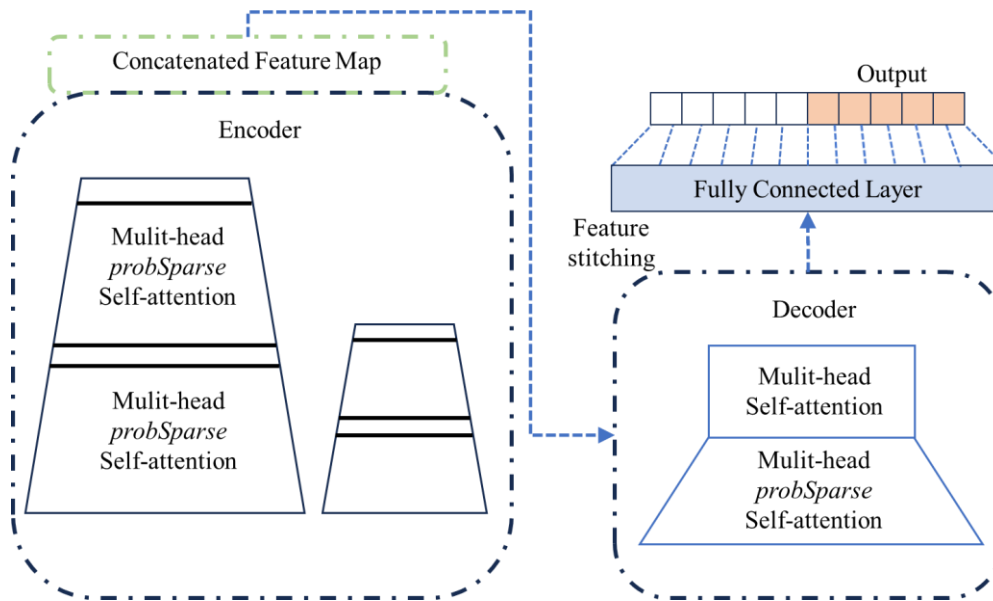
262 3.4 informer

263 informer is an improved and optimized version based on Transformer, specifically designed to
 264 enhance the speed and efficiency of processing long sequences and optimized for long-term time
 265 series prediction tasks (Zhou et al., 2021b). Transformer captures relationships between different
 266 positions in sequences through Self-Attention mechanisms. However, Transformer encounters
 267 difficulties when processing long time series data because its computational complexity grows
 268 quadratically with sequence length, becoming very slow or even unprocessable when dealing with
 269 very long time series.

270 informer proposes ProbSparse Self-attention to filter critical queries and reduce computational
 271 complexity, and introduces Self-attention Distilling to reduce dimensions and network parameters
 272 (Vaswani et al., 2017). As shown in Fig. 3, the informer architecture consists of an encoder-decoder
 273 structure. Input sequences first undergo convolutional encoding and positional embedding before
 274 being fed into the encoder; the encoder utilizes multi-layer probabilistic sparse self-attention and
 275 distillation operations to extract key information, outputting encoded features. The decoder then
 276 directly generates long sequence predictions under masked self-attention and cross-attention,
 277 followed by fully connected layers mapping to final values.

278 For long sequence prediction, the informer has three advantages: 1. Probabilistic sparse self-
 279 attention reduces time complexity from $O(L^2)$ to $O(L \log L)$, significantly reducing computational
 280 overhead; 2. Self-attention distillation progressively compresses the sequence length layer by layer,

281 simultaneously reducing computation and memory requirements; 3. Generative decoding outputs
 282 complete future sequences at once, avoiding error accumulation caused by step-by-step
 283 extrapolation.



284
 285 Figure 3 The construction of the informer

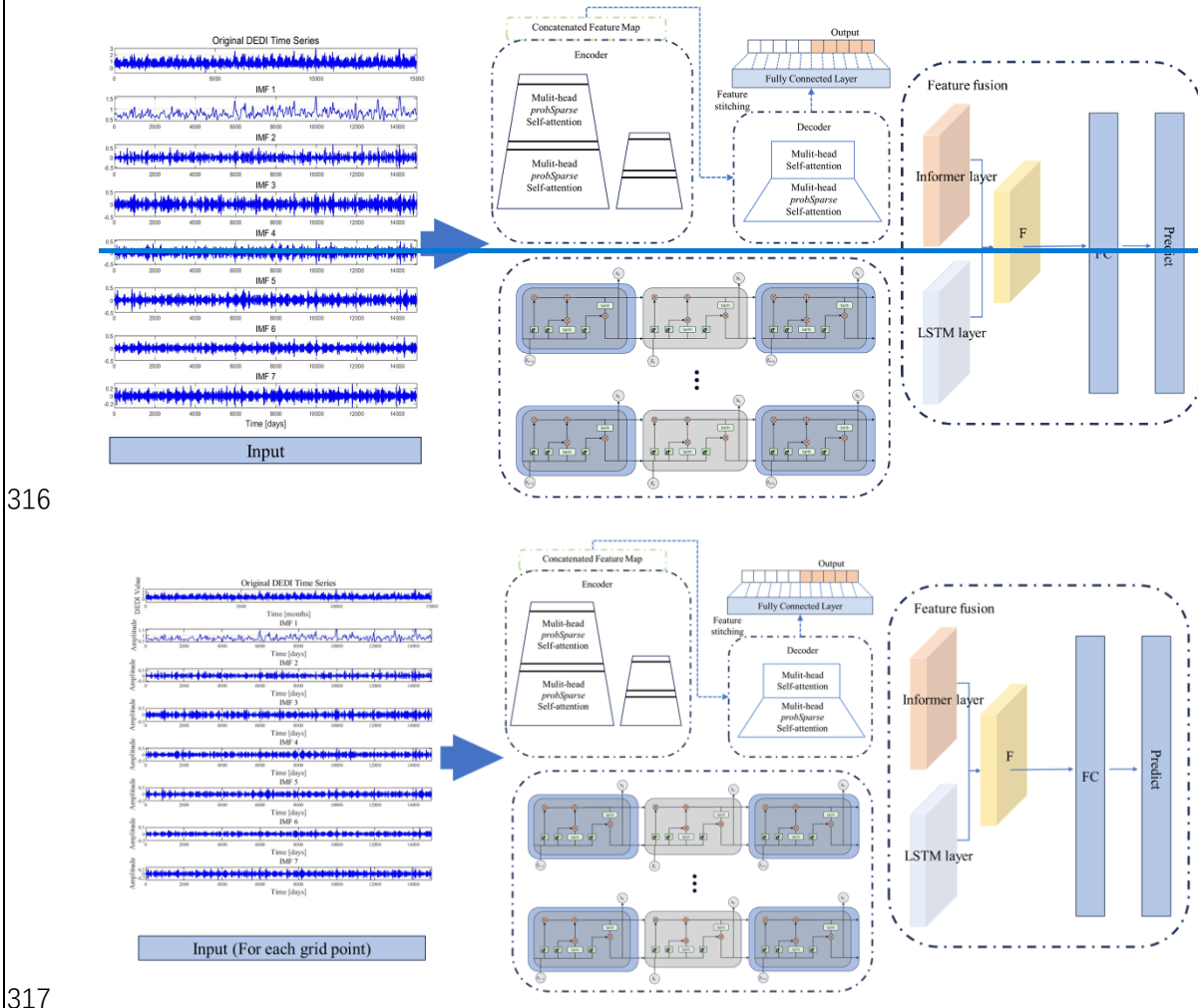
286 3.5 VMD-informer-LSTM

287 The VMD-informer-LSTM model employs Variational Mode Decomposition (VMD) to
 288 deconstruct DEDI time series into multi-frequency scale Intrinsic Mode Functions (IMFs),
 289 achieving the structured extraction of multi-scale features. Based on this foundation, it constructs a
 290 dual-branch parallel architecture of informer and LSTM, where informer efficiently captures global
 291 trends of long-range sequences through probabilistic sparse attention mechanisms, while LSTM
 292 precisely models local temporal dynamics through gate mechanisms. Finally, dual-source features
 293 are fused through fully connected layers to form hybrid feature representations possessing both
 294 long-range dependency analysis capability and short-term fluctuation capture ability. This model
 295 significantly improves prediction accuracy and reliability for complex time series data through a
 296 three-stage design of decomposition-parallelization-fusion, providing an innovative solution for
 297 time series prediction tasks. The construction of VMD-informer-LSTM is shown in Fig. 4 below.

298 Building upon this foundation, in order to ensure the standardization of the model training
 299 process and the reproducibility of the results, this study further establishes a unified design for
 300 dataset partitioning and hyperparameter optimization procedures. For the DEDI time-series data at
 301 each grid point, the dataset is strictly divided in chronological order using a forward-splitting
 302 strategy to prevent any potential leakage of future information. Specifically, the training period
 303 spans from January 1, 1984 to July 3, 2024, while the testing period covers July 4, 2024 to December
 304 31, 2024, which is used to evaluate the model's predictive performance on unseen data over the
 305 subsequent 180-day forecasting horizon. It should be noted that the 180-day prediction in this study
 306 does not correspond to traditional deterministic weather forecasting, but rather focuses on predicting
 307 the evolution of drought states.

308 Regarding hyperparameter configuration, this study adopts the Bayesian Optimization method
 309 to automatically search for key hyperparameters (including hidden layer dimension, learning rate,

310 and batch size) within a predefined parameter search space. Each candidate parameter combination
 311 is evaluated based on its predictive performance on the validation set, with the minimization of
 312 validation error serving as the optimization objective function. The optimal parameter combination
 313 is then selected for the final model training and testing evaluation. Through the design of the above
 314 training strategy and hyperparameter optimization procedure, the experimental process ensures
 315 methodological rigor, stability of results, and reproducibility of the research.



317
 318 Figure 4 The construction of VMD-informer-LSTM

319 3.5 Shapley Additive Explanations

320 Since machine learning models are “black-box” models, although they can provide efficient
 321 predictions, their internal decision-making processes are complex and difficult to intuitively
 322 understand and explain. This may affect result analyses in the field of raster data, which require
 323 transparency and interpretability. To overcome such problems, SHAP values are introduced as an
 324 interpretive method. The SHAP value method was proposed by Lundberg et al (Lundberg & Lee,
 325 2017). In 2017, it is a method based on cooperative game theory that quantifies the contribution of
 326 driving factors to model prediction results. By calculating the marginal contributions of each factor
 327 to the model output under different combinations, it measures their importance in the overall
 328 prediction results. This helps us understand how the model makes decisions. The positive or
 329 negative values of SHAP indicate promotion or inhibition of prediction results. The absolute value

330 reflects the degree of influence of the factor on the model prediction results. The larger the absolute
 331 value, the greater the influence of the factor on model prediction results (Wang et al., 2024). The
 332 formula is as follows:

$$\phi_i = \sum_{S \in N \setminus \{i\}} \frac{|S|! (|N| - |S| - 1)!}{|N|!} [f(S \cup \{i\}) - f(S)] \quad (11)$$

333 In the formula, ϕ_i represents the SHAP value for feature i ; N is the set of all features; S is a
 334 subset of features, excluding feature i ; $f(S)$ is the model output using only the feature subset S for
 335 prediction; ($f(S \cup \{i\})$) is the predicted value after adding feature i to the featured subset S .

336 3.6 Evaluation Metrics

337 The coefficient of determination (R^2) measures the proportion of variance in the dependent
 338 variable that is derived from the independent variable, ranging from 0 to 1, where values closer to
 339 1 indicate better model performance (Nash & Sutcliffe, 1970). The root mean square error (RMSE)
 340 quantifies the average magnitude of prediction errors, providing a measure of how well the model
 341 predicts actual values, with lower values indicating better accuracy (Willmott & Matsuura, 2005).
 342 Mean absolute error (MAE) represents the average absolute difference between predicted and
 343 observed values, offering a linear score that is less sensitive to outliers than RMSE. The range of
 344 mean absolute percentage error (MAPE) is $[0, +\infty]$. A MAPE of 0% indicates a perfect model, while
 345 a MAPE greater than 100% suggests a poor model (Myttenaere et al., 2016).

346 The mathematical expressions for these metrics appear as follows:

$$R^2 = 1 - \frac{SSE}{SST} = 1 - \frac{\sum_{i=1}^N (y_{obs} - y_{pred})^2}{\sum_{i=1}^N \Sigma (y_{obs} - \bar{y}_{obs})^2} \quad (12)$$

$$RMSE = \sqrt{\frac{1}{N} \sum_{i=1}^N (y_{obs} - y_{pred})^2} \quad (13)$$

$$MAE = \frac{1}{N} \sum_{i=1}^N |y_{obs} - y_{pred}| \quad (14)$$

$$MAPE = \frac{1}{N} \sum_{i=1}^N abs\left(\frac{y_{obs} - y_{pred}}{y_{obs}}\right) \quad (15)$$

347 where y_{obs} represents observed values, y_{pred} represents predicted values, \bar{y}_{obs} is the mean of
 348 observed values, and n is the number of observations.

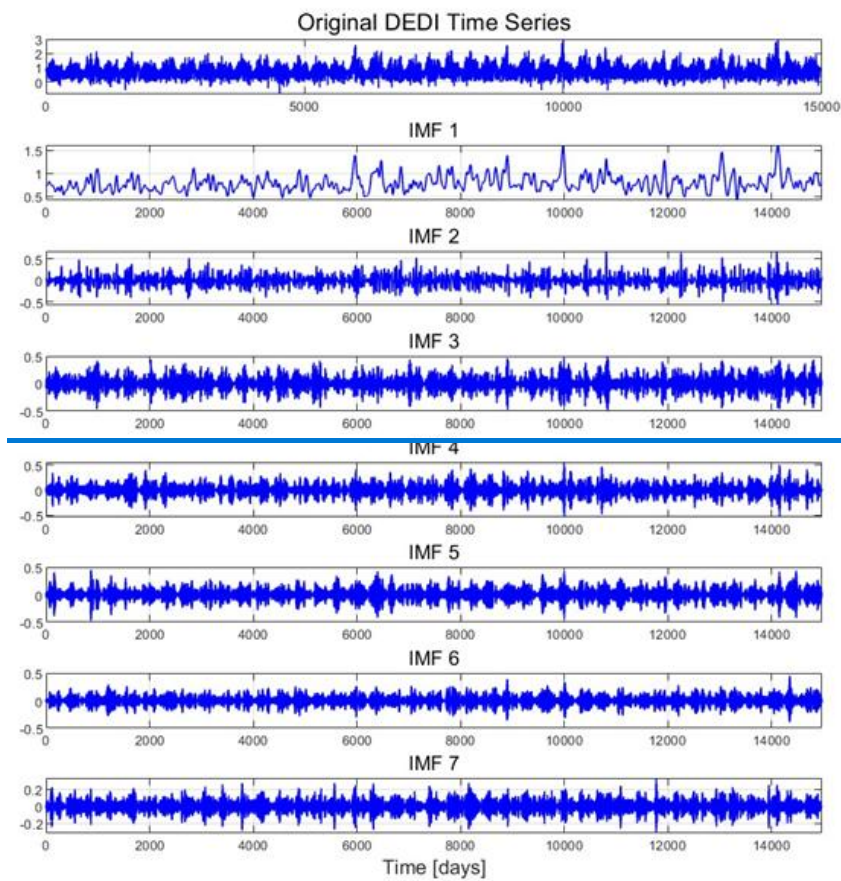
349

350 4. Results

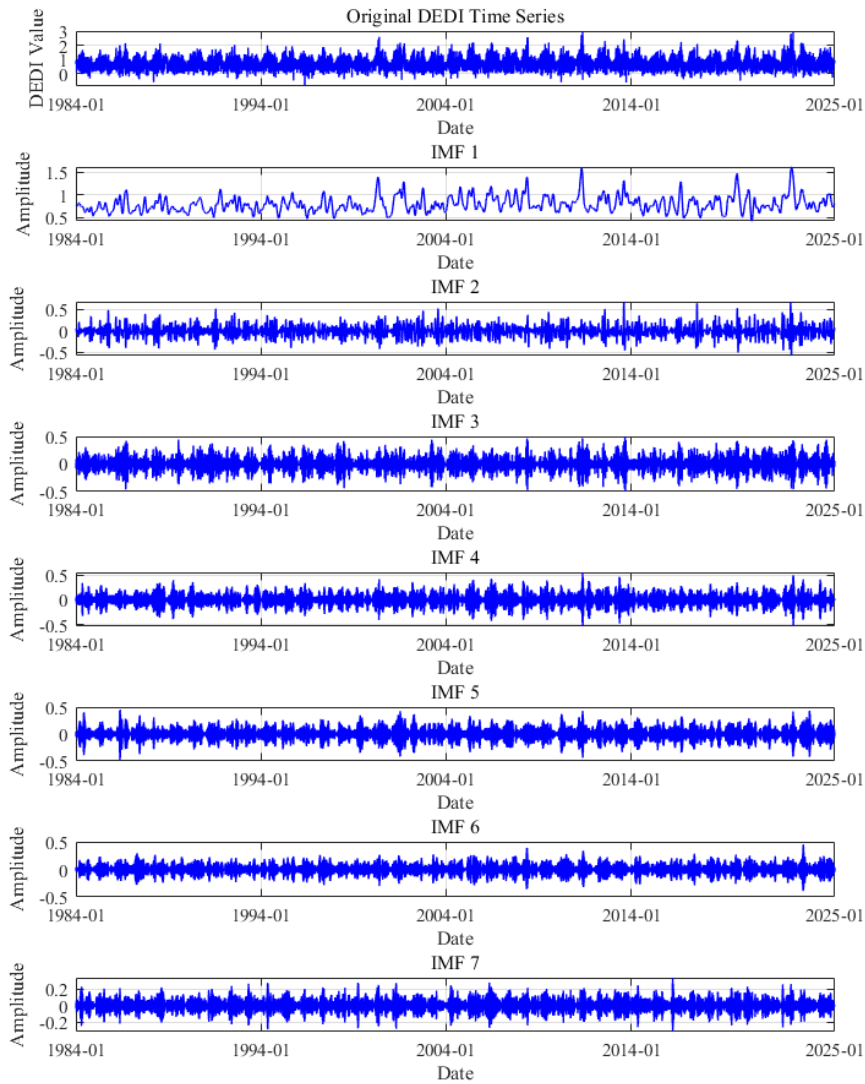
351 4.1 VMD Decomposition Results

352 In this study, we systematically selected 108 grid points distributed across the Huaihe River
 353 Basin and performed VMD analysis of their corresponding daily DEDI time series data spanning
 354 1980-2020. Fig. 5 provides a comprehensive visual representation of the decomposed sub-sequences

355 of DEDI data for a certain representative grid cell in the Huaihe River Basin. As illustrated in Fig.
356 5, the daily DEDI values for a representative grid cell in the Huaihe River Basin exhibit substantial
357 positive and negative fluctuations, with considerable variance between maximum and minimum
358 values. These pronounced oscillations present significant challenges in capturing essential features
359 during the prediction process, as the complex, non-stationary nature of the original signal obscures
360 the underlying patterns and trends. The VMD algorithm successfully decomposes the complex, non-
361 linear DEDI time series into multiple distinct IMFs, each characterized by specific frequency bands
362 and temporal scales. These decomposed components reveal multi-scale variability patterns ranging
363 from high-frequency short-term fluctuations to low-frequency long-term trends, facilitating more
364 effective feature extraction and modeling processes. VMD technology demonstrates superior
365 capability in accurately tracking changes in signal frequency components and effectively revealing
366 the intrinsic and dynamic characteristics of time series, thereby substantially enhancing prediction
367 accuracy and reliability.



368



369

370 Figure 5 The daily DEDI values of a certain grid in the Huaihe River Basin are decomposed into 7
 371 sub - sequence through variational mode decomposition (VMD).

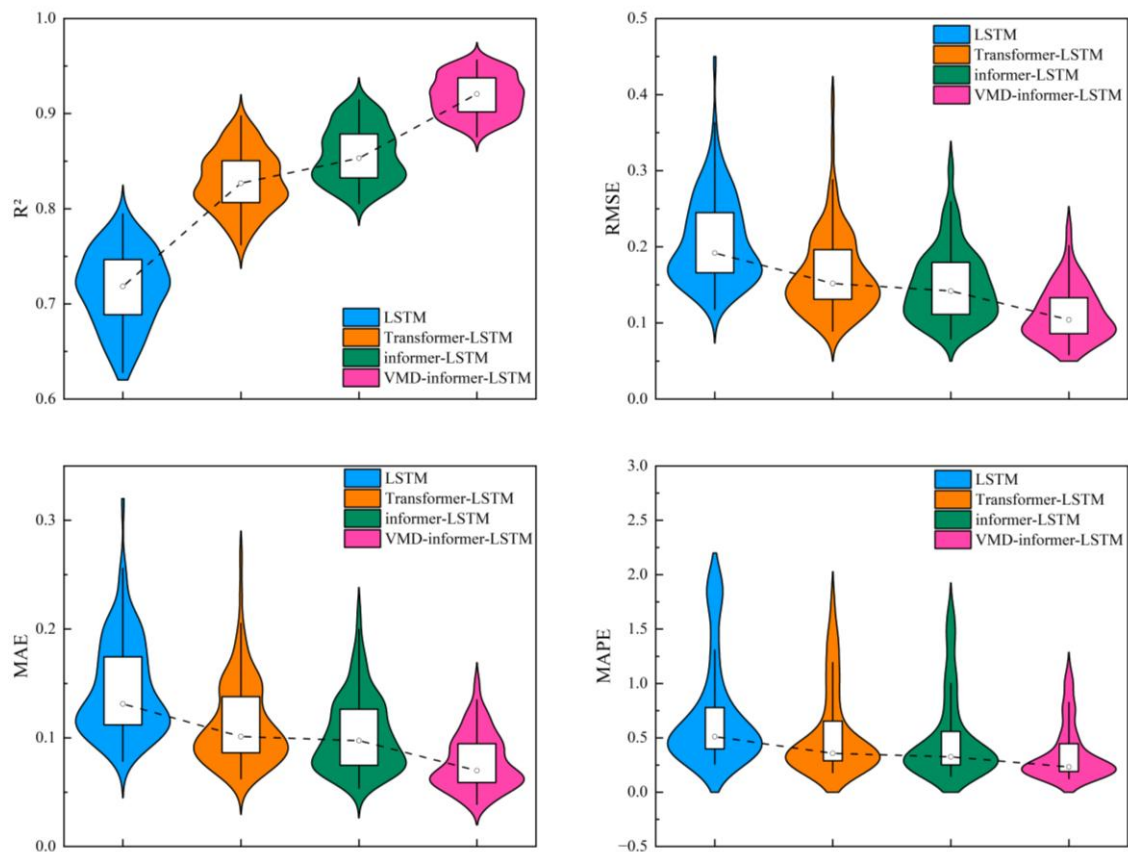
372 4.2 Model Prediction Performance Evaluation

373 To evaluate the performance of the proposed VMD-informer-LSTM model, we performed
 374 extensive comparative experiments involving four distinct modeling approaches: the proposed
 375 VMD-informer-LSTM model, the informer-LSTM model, the Transformer-LSTM model, and the
 376 standalone LSTM model. The evaluation of each model's performance was based on four widely
 377 used statistical metrics for time series prediction evaluation. From Table 1, it can be seen that the
 378 VMD-informer-LSTM model performs the best in terms of predictive performance, with R^2 , RMSE,
 379 MAE, and MAPE reaching 0.9191, 0.1122, 0.0778, and 0.4056, respectively. In contrast, the
 380 informer-LSTM model without VMD decomposition has R^2 , RMSE, MAE, and MAPE of 0.8570,
 381 0.1498, 0.1031, and 0.5330, respectively. After calculation, VMD decomposition improves R^2 ,
 382 RMSE, MAE, and MAPE by 7.25%, 25.10%, 24.54%, and 23.90%, respectively. Furthermore, the
 383 traditional LSTM model shows relatively low predictive accuracy with four evaluation metrics of
 384 $R^2=0.7156$, RMSE=0.2087, MAE=0.1454, and MAPE =0.8254. The Transformer-LSTM model
 385 achieves R^2 , RMSE, MAE, and MAPE of 0.8286, 0.1641, 0.1130, and 0.6266, respectively. This,

386 although better than the basic LSTM model, is still not as good as the informer-LSTM model, let
 387 alone the VMD-informer-LSTM model. In summary, by comparing the predictive performance of
 388 the four models, it is evident that the VMD-informer-LSTM model has an advantage in time series
 389 prediction tasks. Especially after the introduction of VMD decomposition, its performance has
 390 significantly improved, further verifying the effectiveness of VMD decomposition in enhancing
 391 model predictive accuracy.

392 Table 1 Overall average evaluation indicators of various models within the Huaihe River Basin

Indicator	LSTM	Transformer-LSTM	informer-LSTM	VMD-informer-LSTM
R ²	0.7156	0.8286	0.8570	0.9191
RMSE	0.2087	0.1641	0.1498	0.1122
MAE	0.1454	0.1130	0.1031	0.0778
MAPE	0.8254	0.6266	0.5330	0.4056



393
 394 Figure 6 Violin-box plots of evaluation indicators for different models in the Huaihe River Basin

395 Fig. 6 presents violin plots illustrating the distribution of evaluation metrics across all 108 grid
 396 points in the Huaihe River Basin. This provides insights into model performance variability and
 397 consistency. Violin plots reveal important patterns. The VMD-informer-LSTM model demonstrates
 398 the most concentrated distribution around optimal values, with R² distributions tightly clustered near
 399 0.92-0.95, indicating consistent and high performance across diverse geographical locations. Error
 400 metric distributions (RMSE, MAE and MAPE) show the VMD-informer-LSTM model has the
 401 narrowest spread and the lowest median values, suggesting robust prediction accuracy with minimal
 402 spatial variability.

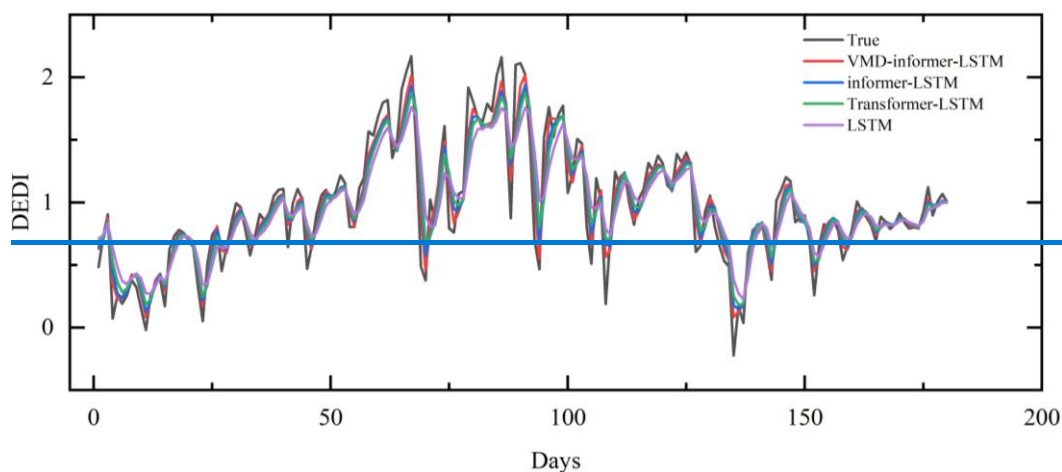
403 The RMSE distributions demonstrate a clear monotonic improvement from LSTM (median:

404 0.2087) through Transformer-LSTM (0.1641), informer-LSTM (0.1498) to VMD-informer-LSTM
405 (0.1122), with progressively narrower interquartile ranges and fewer outliers. The VMD-informer-
406 LSTM model exhibits the most concentrated distribution with minimal dispersion (IQR: 0.05),
407 indicating superior prediction accuracy and enhanced stability across diverse geographical locations.
408 This concentrated performance distribution reflects the effectiveness of combining VMD
409 decomposition with hybrid deep learning architectures for robust drought prediction.

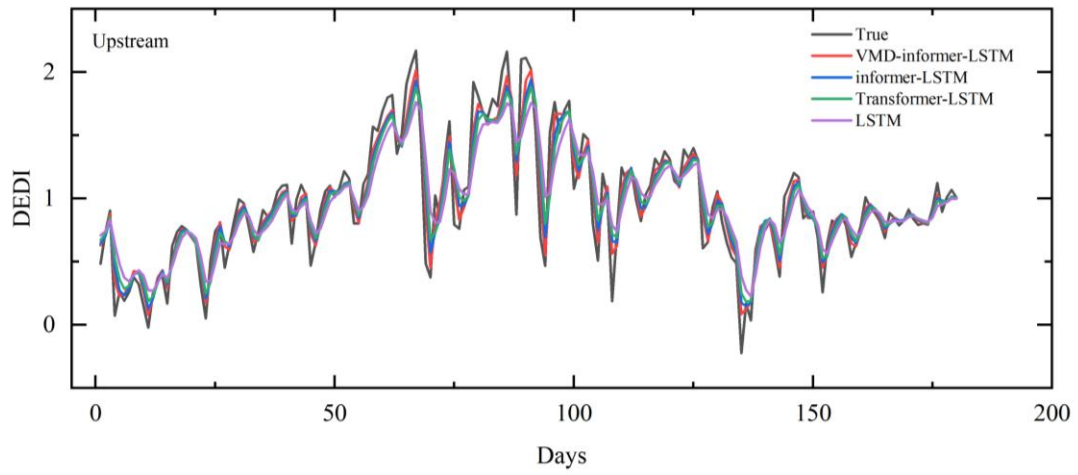
410 Comparing the four models, the VMD-informer-LSTM model consistently outperforms the
411 other three, with spatially averaged performance metrics across all 108 grid points in the Huaihe
412 River Basin, including an R^2 of 0.9191, RMSE of 0.1122, MAE of 0.0778, and MAPE of 0.4056.
413 The informer-LSTM model without VMD decomposition has spatially averaged metrics across all
414 grid points of $R^2 = 0.8570$, RMSE = 0.1498, MAE = 0.1031, and MAPE = 0.5330. The Transformer-
415 LSTM model achieves spatially averaged metrics of $R^2 = 0.8286$, RMSE = 0.1641, MAE = 0.1130,
416 and MAPE = 0.6266, while the basic LSTM model shows the lowest performance, with spatially
417 averaged metrics of $R^2 = 0.7156$, RMSE = 0.2087, MAE = 0.1454, and MAPE = 0.8254.

418 ~~Comparing the four models, the VMD-informer-LSTM model consistently outperforms the~~
419 ~~other three, with an average R^2 of 0.9191, RMSE of 0.1122, MAE of 0.0778, and MAPE of 0.4056.~~
420 ~~The informer-LSTM model without VMD decomposition has an average R^2 of 0.8570, RMSE of~~
421 ~~0.1498, MAE of 0.1031, and MAPE of 0.5330. The Transformer-LSTM model achieves an average~~
422 ~~R^2 of 0.8286, RMSE of 0.1641, MAE of 0.1130, and MAPE of 0.6266. The basic LSTM model has~~
423 ~~the lowest performance, with an average R^2 of 0.7156, RMSE of 0.2087, MAE of 0.1454, and~~
424 ~~MAPE of 0.8254.~~

425 The performance improvement from LSTM to Transformer-LSTM to informer-LSTM is
426 evident, with each model showing better median values and reduced spread in the error metrics
427 compared to the previous one. However, the VMD-informer-LSTM model stands out with the most
428 significant enhancements in both median performance and reduced variance across all metrics. This
429 indicates that the integration of VMD decomposition with the informer-LSTM architecture provides
430 the most substantial benefits in terms of prediction accuracy and consistency.



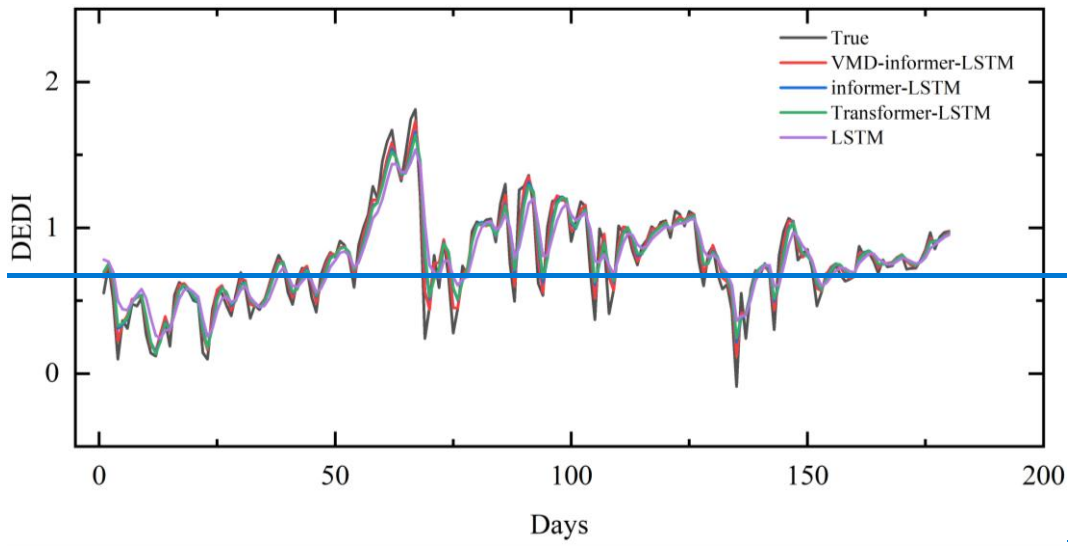
431



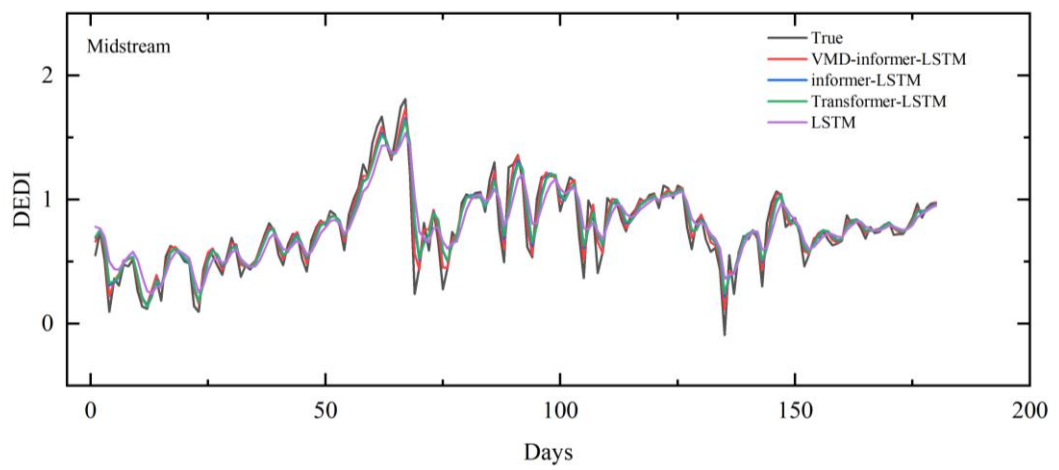
432

433

(a)



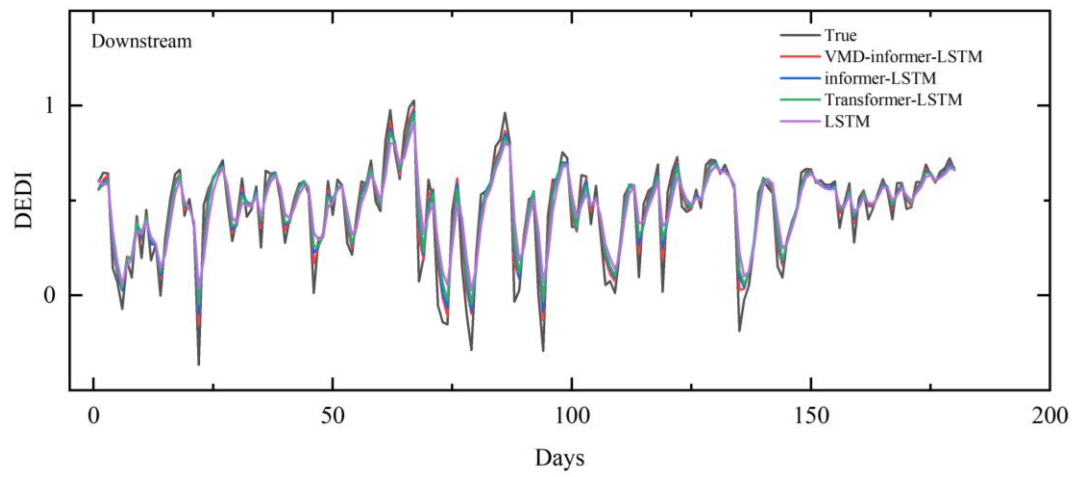
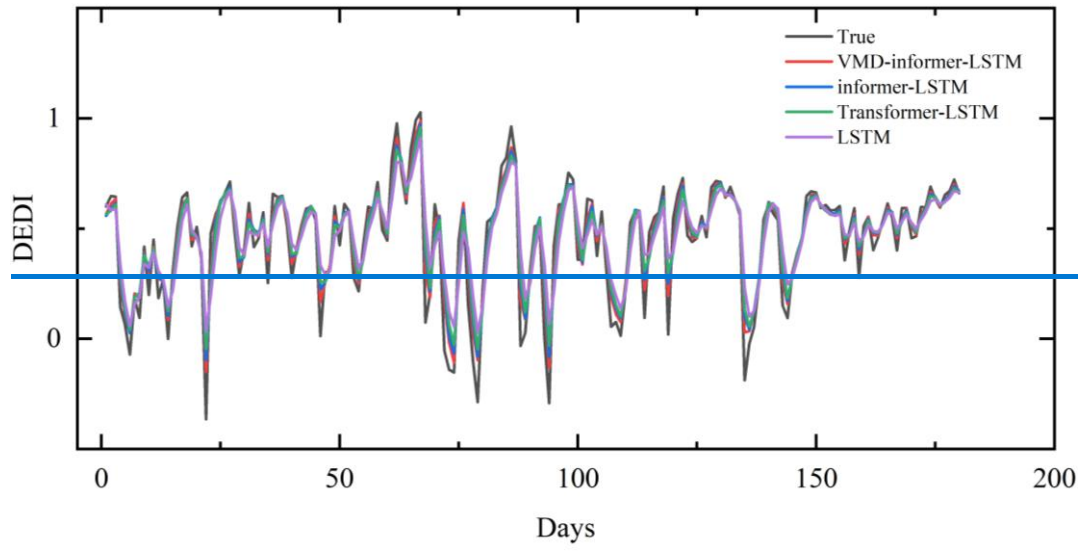
434



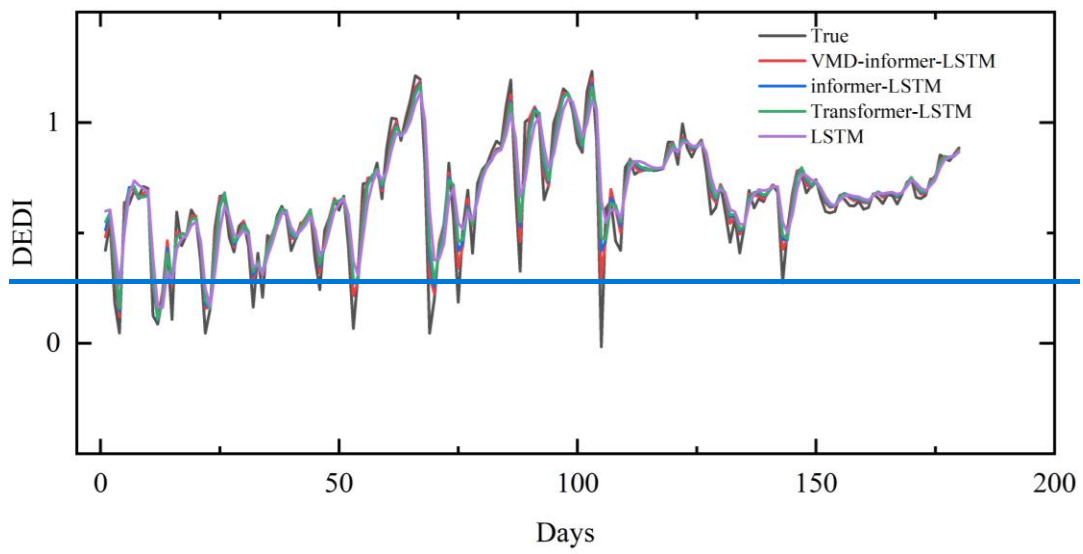
435

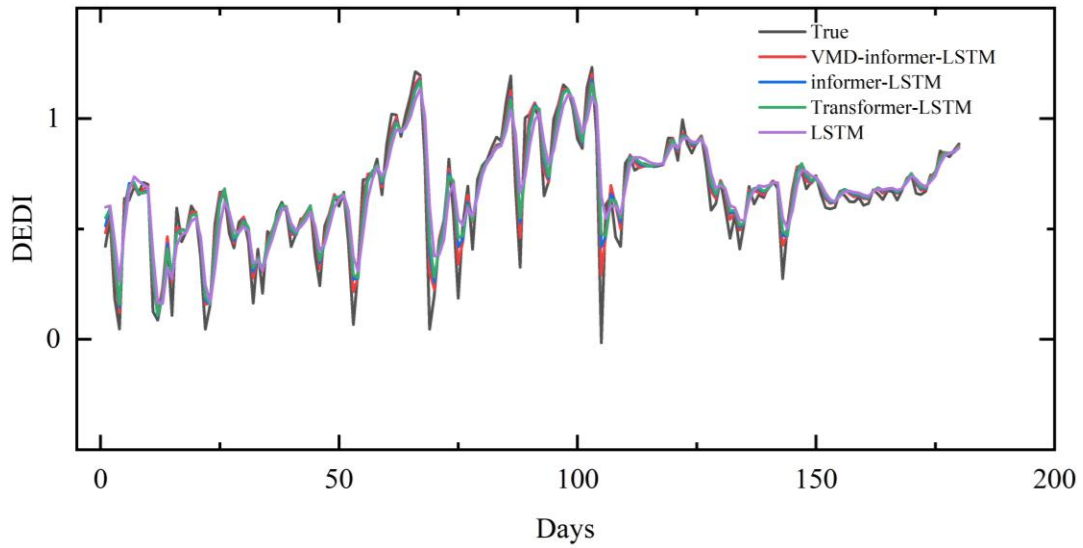
436

(b)



(c)





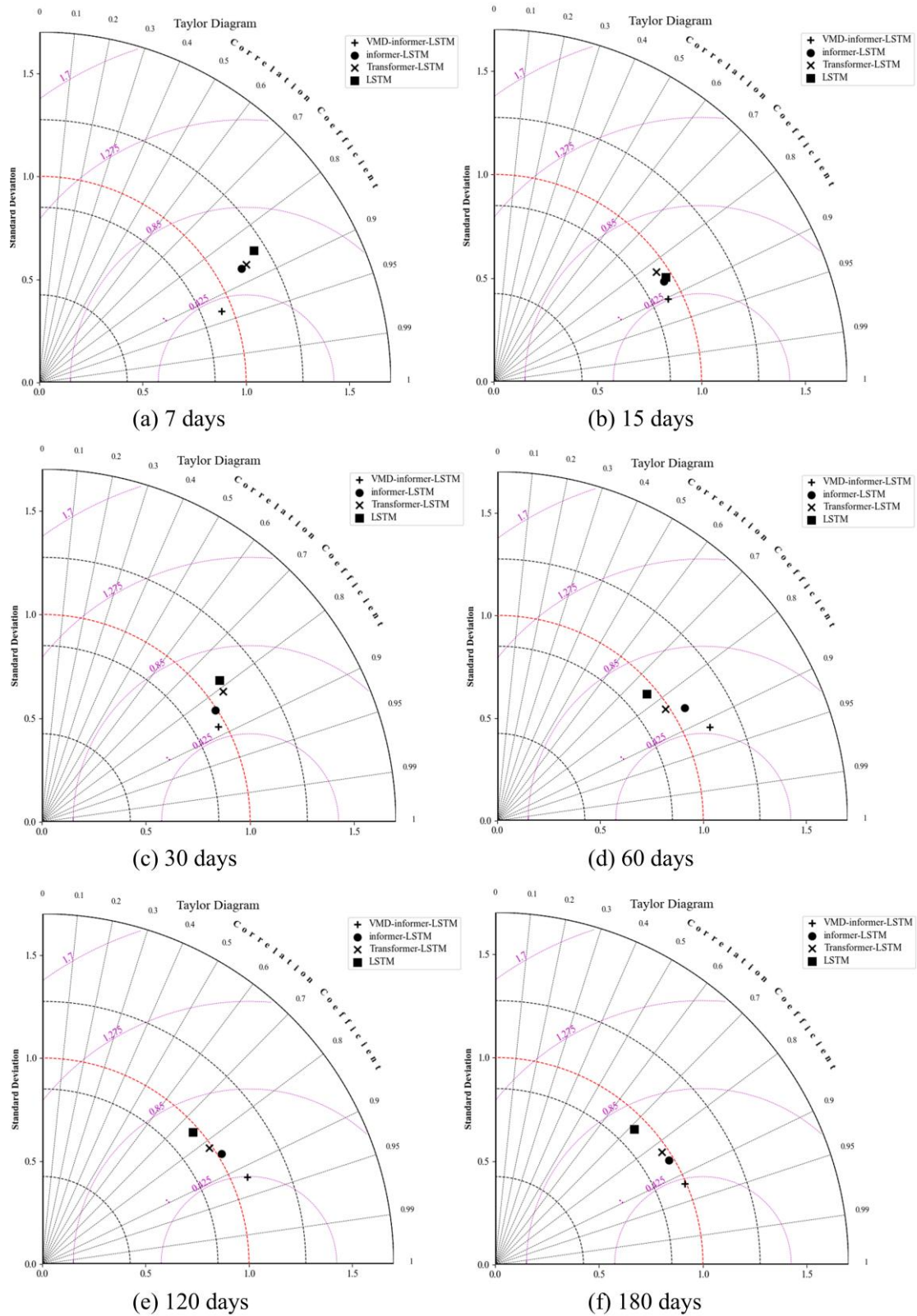
(d)

Figure 7 Line charts of different models' 180 - day predictions in four Huaihe River Basin

Regions: (a) Upstream; (b) Midstream; (c) Downstream; (d) Yi Shu Si River

Fig. S1 and Fig. 7 show scatter plots and line charts of different models' 180-day predictions in different Huaihe River Basin regions. As illustrated in Fig. S1, LSTM yields the lowest R^2 values (0.76–0.78) across all subplots and is therefore the poorest performer; its scatter points visibly diverge from the 1:1 line, reflecting the largest prediction errors. Although informer-LSTM is less accurate than VMD-informer-LSTM, it maintains a stable R^2 of about 0.89, and the scatter deviation is markedly smaller than those of Transformer-LSTM and LSTM.

Fig. 7 further indicates that all four models successfully capture the overall drought trend, yet differ in precision. When the line plots are examined in conjunction, it becomes clear that VMD-informer-LSTM outperforms the other three models, delivering superior agreement between simulated and ERA5 reanalysis values, higher prediction accuracy, and the best overall performance. informer-LSTM and Transformer-LSTM rank next, whereas LSTM only roughly reproduces the drought trend and performs poorly at predicting extremes, resulting in the lowest predictive capability.



459

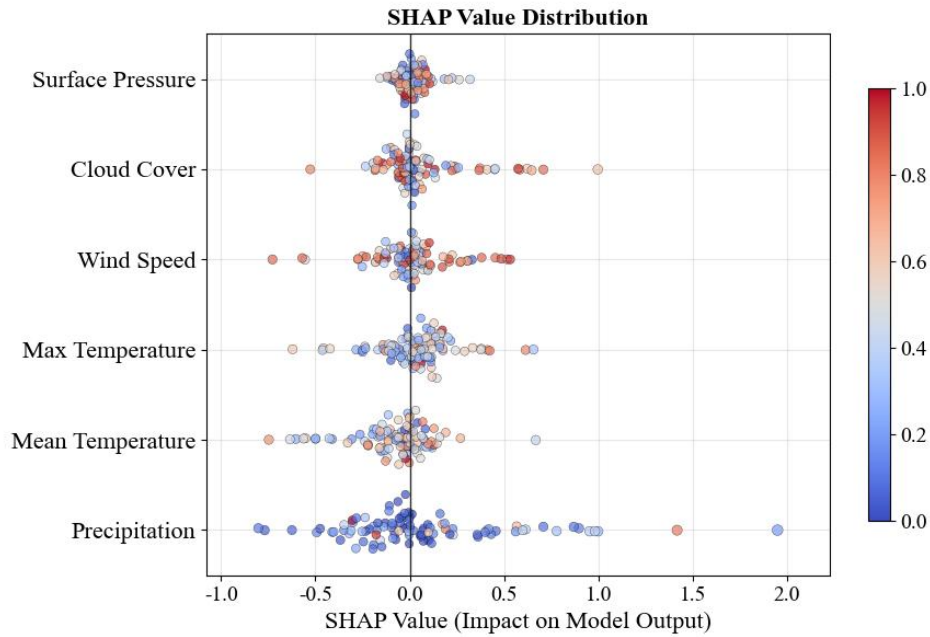
460 Figure 8 Taylor diagrams comparing the performance of different models for DEDI prediction in
 461 the Huaihe River Basin at different lead times: (a) 7 days; (b) 15 days; (c) 30 days; (d) 60 days; (e)
 462 120 days; (f) 180 days.

463 Fig. 8 presents Taylor diagrams that evaluate the predictive performance of various models
 464 across different lead times: (a) 7 days, (b) 15 days, (c) 30 days, (d) 60 days, (e) 120 days, and (f)

465 180 days. These diagrams provide a comprehensive assessment by integrating standard deviation
466 and correlation coefficients from the ERA5 reanalysis data. The VMD-informer-LSTM model
467 consistently shows superior predictive accuracy across all lead times, with its predictions closely
468 aligned with the ERA5 reanalysis data, particularly in the upper, middle, and lower regions of the
469 Huaihe River Basin and the Yi Shu Si River regions. At short lead times (7 and 15 days), all models
470 perform relatively well, but the VMD-informer-LSTM model slightly outperforms the others. As
471 the lead time extends to 30 and 60 days, the VMD-informer-LSTM model maintains high accuracy
472 while other models show performance degradation, indicating a reduced ability to capture the
473 underlying data patterns effectively. At long lead times (120 and 180 days), the VMD-informer-
474 LSTM model's advantage becomes more pronounced, with its predictions remaining significantly
475 closer to the ERA5 reanalysis data than other models, which exhibit more noticeable divergence.
476 This suggests that the VMD-informer-LSTM model is better equipped to handle the increased
477 uncertainty and complexity associated with long-term predictions, highlighting its robustness and
478 reliability in predictive tasks, especially crucial in drought forecasting where lead time is a critical
479 factor.

480 4.3 Model Influencing Factor Analysis

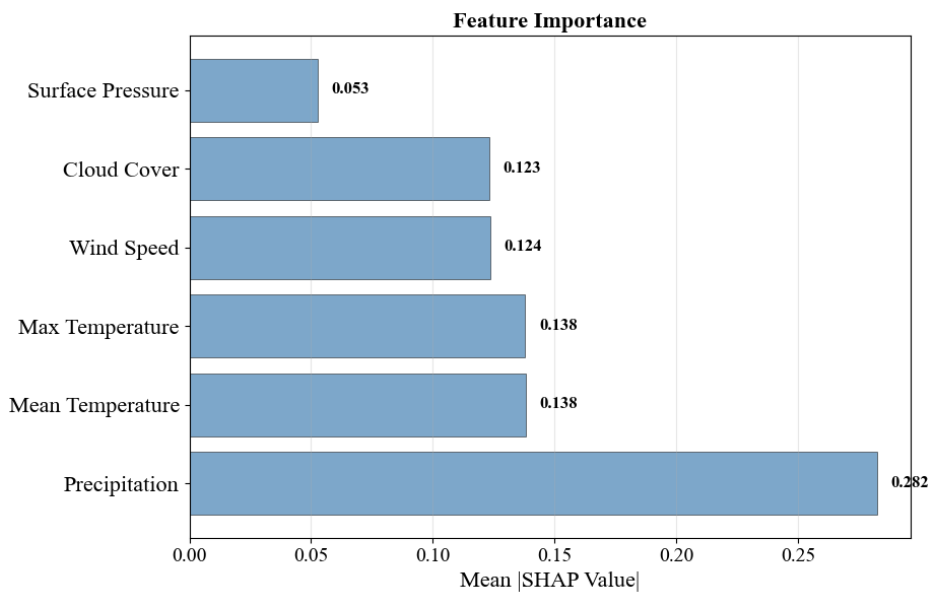
481 Fig. 9a presents a comprehensive SHAP value distribution analysis revealing the complex,
482 non-linear relationships between meteorological variables and drought prediction outcomes.
483 Precipitation emerges as the dominant predictor with predominantly positive SHAP contributions,
484 indicating its critical role in alleviating drought conditions through direct water supply augmentation.
485 However, the wide distribution of precipitation SHAP values (-1.00 to 2.00) suggests threshold-
486 dependent effects, where low precipitation events contribute negatively to drought mitigation while
487 high precipitation provides substantial positive contributions. Temperature exhibits a more complex
488 influence pattern, with SHAP values distributed across both positive and negative domains,
489 reflecting its dual role in drought dynamics: moderate temperatures may enhance vegetation water
490 use efficiency (positive contribution), while extreme temperatures intensify evapotranspiration
491 demands and soil moisture depletion (negative contribution). Fig. 9b quantifies that precipitation
492 and mean temperature collectively account for approximately 49.00% of the total model decision-
493 making process, with average SHAP magnitudes of 0.282 and 0.138 respectively. Surface pressure,
494 cloud cover, and maximum temperature demonstrate moderate but consistent influences (SHAP
495 magnitudes of 0.053 to 0.124), likely operating through indirect pathways affecting atmospheric
496 moisture transport, radiation balance, and boundary layer dynamics. The concentrated distribution
497 of these secondary variables' SHAP values suggests more linear, predictable relationships with
498 drought outcomes, contrasting with the high variability observed in precipitation and temperature
499 effects, which reflects the non-stationary nature of hydro-climatic processes and the model's
500 capacity to capture complex feature interactions across different drought severity conditions.



501

502

(a)



503

504

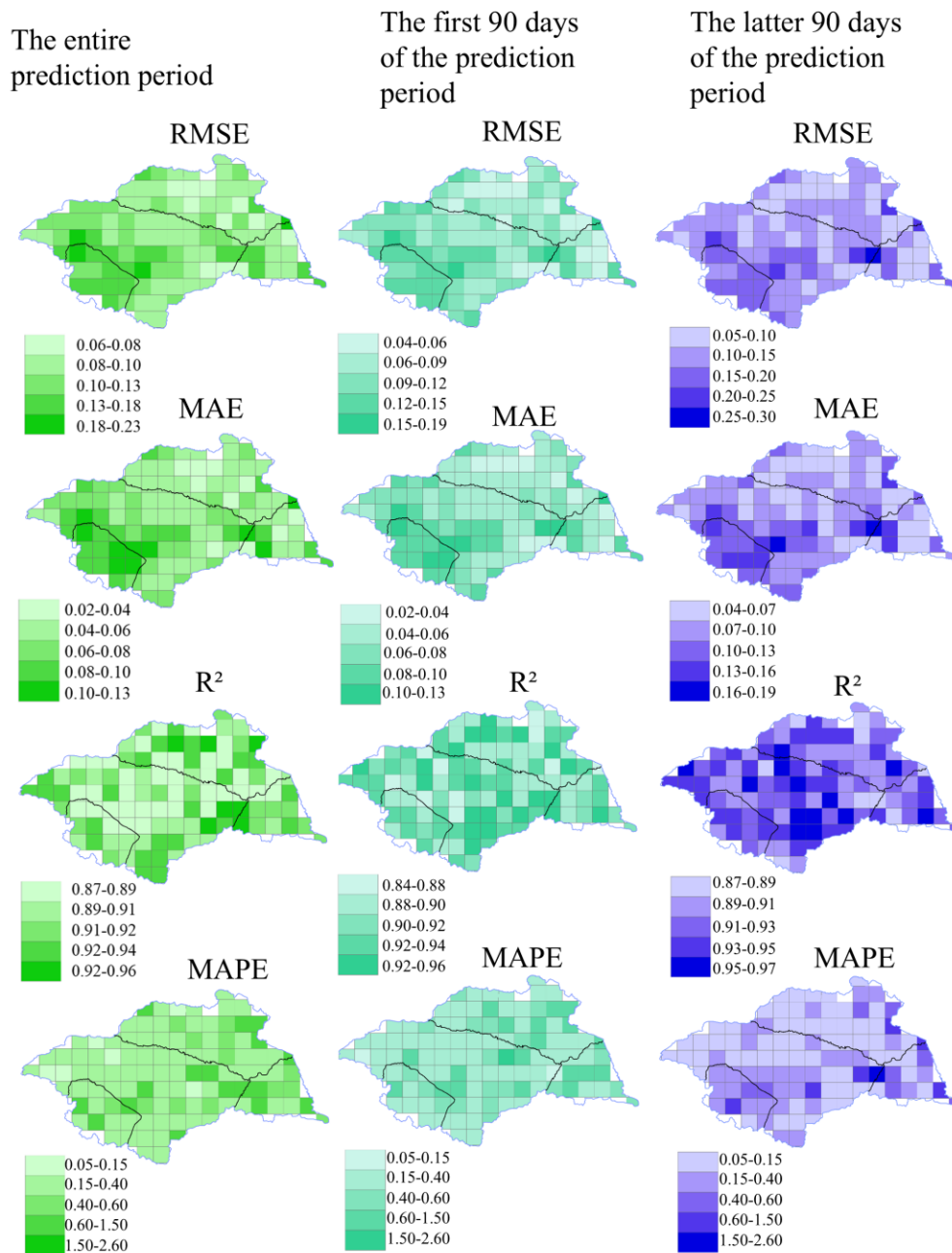
(b)

505 Figure 9 Relative contributions of meteorological variables to drought forecasting at a 180-day
506 lead time

507 While this study demonstrates the superior performance of the VMD-informer-LSTM model
508 through comprehensive comparative analysis, several aspects of model uncertainty warrant
509 acknowledgement. The concentrated performance distributions observed in violin plots suggest
510 relatively low model uncertainty across different geographical locations, with the VMD-informer-
511 LSTM model showing the most stable performance (IQR: 0.05 for RMSE). However, systematic
512 uncertainty quantification through techniques such as ensemble modeling, Monte Carlo dropout, or
513 Bayesian approaches was not implemented in this study, representing a limitation that could be
514 addressed in future research to provide confidence intervals for predictions and better understand
515 prediction reliability under different hydroclimatic conditions.

516 The spatial analysis reveals that prediction accuracy varies across the basin, with slightly
517 higher uncertainties observed along catchment peripheries. This is potentially related to boundary
518 effects or data quality variations. Future work should incorporate explicit uncertainty quantification
519 methods to enhance the model's operational applicability and provide decision-makers with
520 confidence measures alongside drought predictions.

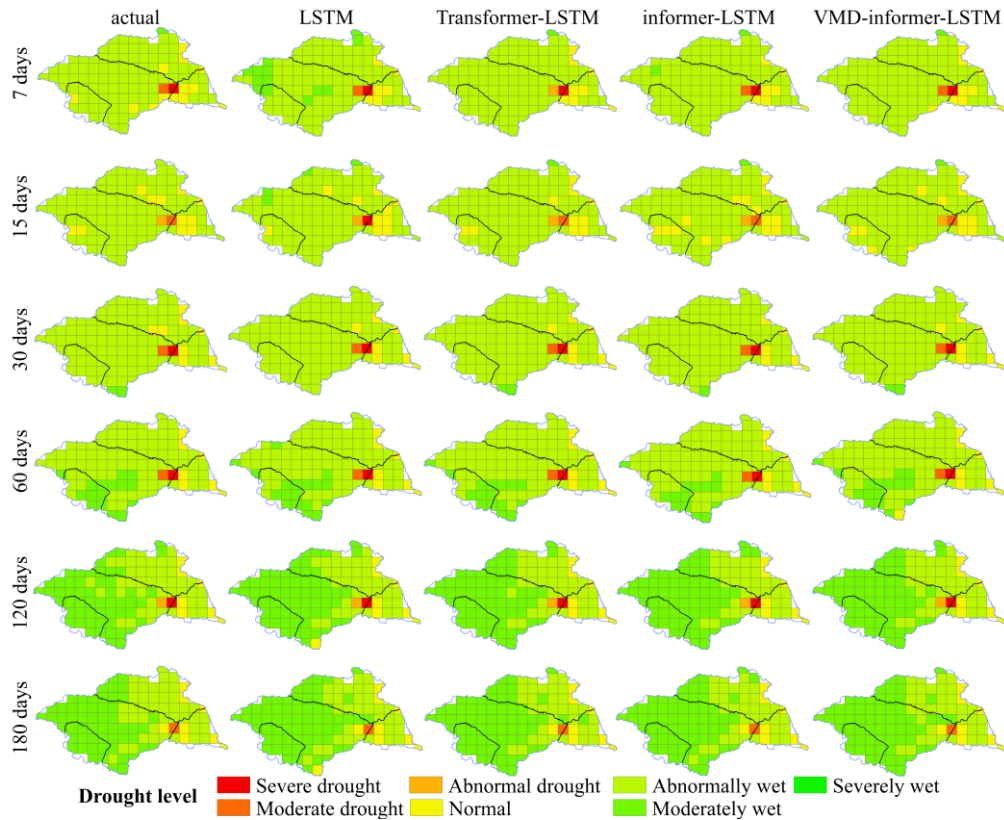
521 Fig. 10 illustrates the spatial prediction performance of the VMD-informer-LSTM model in
522 the Huaihe River Basin. Overall, the model achieves the highest accuracy in the first 90 days of
523 prediction, with an R^2 close to 0.92 and low error, effectively characterizing the evolution of drought.
524 As the prediction horizon extends beyond 90 days, the accuracy shows a noticeable decline,
525 reflecting the increasing difficulty of capturing long-term drought dynamics. In terms of spatial
526 distribution, the upstream area performs the best, accurately reproducing the observed drought
527 process. The downstream area follows, with the overall drought trend being tracked, though there
528 is a tendency of underestimation in drought intensity. The midstream area shows slightly larger
529 errors, but maintains high consistency with ERA5 reanalysis data on a long-term scale. The Yi Shu
530 Si River region shows a relatively balanced performance, with the model effectively reflecting
531 changes in drought levels.



532

533

Figure 10 The spatial distribution of VMD-informer-LSTM Model performance



534

535

Figure 11 Comparison of drought forecasting model performance at different time scales

536

537

Fig. 11 further reveals the characteristics of drought category distribution under different prediction horizons and reflects regional differences. In the short-term predictions (first 15 days), although some models exhibit prediction errors, the overall results in the upstream, midstream, downstream, and Yi Shu Si River regions remain broadly consistent with observations. At the 7-day horizon, the LSTM misclassifies 11 grid cells, identifying the abnormally wet category as moderately wet. At 15 days, the informer-LSTM shows errors in 4 grid cells, misclassifying abnormally wet conditions as normal.

538

539

540

541

542

543

In the medium-term predictions (30–60 days), the VMD-informer-LSTM demonstrates the best performance, with only 2 misclassified grid cells at both horizons, whereas the other three models show larger deviations, mainly concentrated in the upstream, midstream, and Yi Shu Si River regions. In the long-term predictions (120–180 days), prediction errors increase across all models; however, the VMD-informer-LSTM continues to maintain the highest overall accuracy. Across all prediction periods, models exhibit a common tendency to underestimate drought categories, with the VMD-informer-LSTM showing the smallest degree of underestimation.

544

545

546

547

548

549

550

Overall, it can be seen that the upstream and downstream regions achieved the highest observations consistency, followed by the Yi Shu Si River region, while the midstream region performed the weakest.

551

552

533 5. Discussion

554

555

556

557

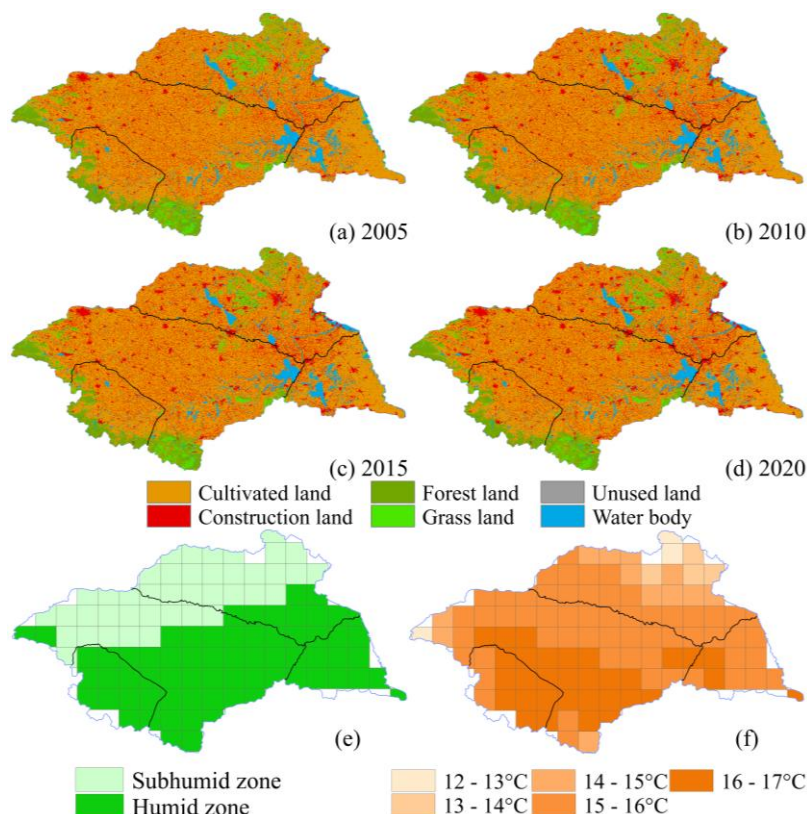
Further combining Table 2 and Fig. 12 provides a clearer understanding of the reasons for the differences in model prediction accuracy across different regions. From 2005 to 2020, the cultivated land in the basin continuously decreased (from 187,254 km² to 180,161 km²), the construction land significantly increased (from 34,739 km² to 42,801 km²), the grassland area markedly declined, and

558 the water area slightly increased. In the midstream region, the reduction of cultivated land, forest
 559 land, and grassland, coupled with the increase in construction land leading to the expansion of
 560 impervious surfaces, has altered the water cycle process. This has caused the model's prediction to
 561 underestimate drought severity, demonstrating that environmental changes have exacerbated
 562 hydrological droughts.

563

Table 2 Area of land use types in Huaihe River basin from 2005 to 2020(km²)

Year	Cultivated Land	Forest land	Grassland	Water Body	Building	Unused Land
2005	187254	16550	10149	13159	34739	213
2010	186078	16593	10117	13224	35841	212
2015	184597	16539	10049	13326	37326	231
2020	180161	16052	8083	14282	42801	168



564

565 Figure 12 Distribution of Land Use, Climate Zones, and Multi-year Average Temperature in
 566 the Huaihe River Basin (a)–(d) Spatiotemporal distribution of land use in the Huaihe River Basin
 567 from 2005 to 2020; (e) Distribution map of semi-humid and humid zones in the Huaihe River
 568 Basin; (f) Distribution map of multi-year average temperature in the Huaihe River Basin

569 Meanwhile, Figure 12 shows distinct climatic zone characteristics: the upstream, southern
 570 midstream, downstream, and southern regions of the Yi Shu Si River are in the humid zone, where
 571 the annual mean temperature in the upstream and its adjacent southern midstream regions is close
 572 to 17°C, and the annual mean temperature in the downstream and its adjacent southern midstream
 573 regions as well as the southern regions of the Yi Shu Si River is between 13–16°C. In contrast, the
 574 northern midstream and northern regions of the Yi Shu Si River are in the semi-humid zone, with
 575 an annual mean temperature between 12°C and 15°C. Overall, the prediction results of several
 576 models underestimated hydrological drought, with misclassifications mainly concentrated in the
 577 transition zones between the humid and semi-humid regions. The semi-humid regions showed

578 relatively more frequent errors compared to the humid regions.

579 The results show that the VMD–Informer–LSTM model exhibits high prediction accuracy
580 within the 30–90 day forecast period at the time scale, while the prediction accuracy decreases
581 during the longer forecast period of 120–180 days. Spatially, the prediction results for the upstream
582 and downstream regions show the highest consistency with the ERA5 reanalysis values, followed
583 by the Yishuisi River region, with the midstream region showing relatively weaker performance. In
584 summary, the VMD–Informer–LSTM framework proposed in this study demonstrates significant
585 advantages in handling drought index series with prominent non-stationarity and multi-time scale
586 features, using a multi-scale modeling strategy of "decomposition—parallel modeling—feature
587 fusion." On the one hand, VMD effectively reduces the complexity of the original series, allowing
588 for the separation of variation features at different time scales and modeling them individually. On
589 the other hand, the parallel structure of Informer and LSTM focuses on capturing long-term
590 background state changes and short-term fluctuations, enabling the model to represent both the
591 persistence and phase-specific fluctuations of the drought process.

592 However, this study still has certain limitations. First, the model evaluation is primarily based
593 on ERA5 time-series data and lacks generalization validation using independent observations or
594 multi-source remote sensing data. Second, the model is constructed using one-dimensional time
595 series at individual grid points as input, without explicitly capturing the spatial propagation of
596 drought, thereby neglecting the spatial interconnections among different regions. Despite these
597 limitations, the proposed framework still demonstrates considerable potential in evaluating the
598 evolution of drought background conditions and can provide useful support for medium- to long-
599 term water resource regulation and risk assessment at the basin scale. Future work will incorporate
600 multi-source observational data and develop spatiotemporal coupling modeling approaches to
601 enhance the representation of drought evolution processes, thereby improving the reliability of
602 predictions.

603

604 6. Conclusion

605 This study takes the Huaihe River Basin in China as an example and constructs the VMD-
606 informer-LSTM model, and compares it with the LSTM, Transformer-LSTM, and informer-LSTM
607 models to verify its ability to predict hydrological drought in both temporal and spatial dimensions,
608 and influencing factors are quantitatively analyzed. The main conclusions are as follows:

609 (1) The VMD-informer-LSTM model shows clear advantages in drought forecasting across
610 different lead times and drought severity levels. Compared with the baseline LSTM, it improves R^2
611 by 28.4% ($0.7156 \rightarrow 0.9191$) and reduces RMSE by 46.2% ($0.2087 \rightarrow 0.1122$). Further
612 comparisons reveal that the single LSTM struggles to capture the complex drought process and
613 performs the poorest in all models' predictions. Transformer-LSTM improves accuracy to some
614 extent, but there is still significant error accumulation in long-term predictions. The informer-LSTM,
615 leveraging the sparse self-attention mechanism and generative decoding approach of the informer,
616 can balance efficiency and accuracy in long time series prediction, showing greater stability than
617 Transformer-LSTM and being the best among the three benchmark models. However, the VMD-
618 informer-LSTM, by introducing VMD decomposition to further extract multi-scale features and
619 combining the long sequence modeling advantages of the informer with the local dynamic
620 characterization ability of LSTM, achieves multi-level information fusion. Therefore, the VMD-

621 informer-LSTM model achieves the highest precision in short-term forecasting (7 days), has the
622 smallest error growth rate in the medium term (30–60 days), and can still more effectively
623 characterize the evolution of drought in the long term (120–180 days). Its underestimation of
624 drought intensity is significantly lower than other models.

625 (2) The spatial prediction performance of the VMD informant LSTM model is influenced by
626 land use and climate regions. Within the entire watershed, all models showed excellent prediction
627 performance within a 30 day prediction period, with the VMD-informer-LSTM model being the
628 most accurate. However, within a prediction period of 120-180 days, the prediction accuracy of all
629 models significantly decreased throughout the watershed. Overall, the predicted drought intensity
630 was relatively mild, with misclassifications mainly concentrated in the transition zones between the
631 humid and semi-humid regions, and errors occurring more frequently in the semi-humid regions
632 compared to the humid regions. The model performs best in the upstream region, followed by the
633 downstream and Yishus River regions, while prediction accuracy in the midstream region is
634 relatively weak. With the extension of the forecast lead time, this downward trend is most evident
635 in the middle reaches, where the reduction of arable land, grassland, and forest land, as well as the
636 expansion of construction land, have changed the water cycle process, indicating that human
637 activities have exacerbated drought.

638 (3) The SHAP analysis enhances the interpretability of the VMD-informer-LSTM model by
639 revealing the relative importance of meteorological variables in drought prediction. Precipitation is
640 the dominant factor, contributing about 28.2% to model decisions, followed by mean temperature
641 (13.8%), while surface pressure, cloud cover, and maximum temperature together account for about
642 15–20%. These results confirm that the model effectively identifies key meteorological drivers and
643 enhances the interpretability of drought forecasting.

644 Author Contributions:

645 Conceptualization: Min Li, Ming Ou, Yuhang Yao, Changman Yin

646 Data curation: Ming Ou

647 Formal analysis: Min Li, Ming Ou

648 Funding acquisition: Min Li

649 Investigation: Min Li, Ming Ou

650 Methodology: Min Li, Ming Ou

651 Software: Min Li

652 Supervision: Ming Ou, Yuhang Yao, Changman Yin

653 Validation: Min Li

654 Visualization: Ming Ou, Yuhang Yao, Changman Yin

655 Writing – original draft: Min Li, Ming Ou

656 Writing – review & editing: Yuhang Yao, Changman Yin

657 Declaration of competing interest

658 The authors declare no conflicts of interest relevant to this study.

659 Data Availability Statement

660 The gridded daily precipitation, evaporation, potential evaporation, mean temperature,
661 maximum temperature, cloud cover, surface pressure, and wind speed data with a spatial r

662 resolution of 0.25° were obtained from ERA5 post-processed daily statistics on single level
663 s from 1940 to present (<https://cds.climate.copernicus.eu/datasets/derived-era5-single-levels-daily-statistics?tab=overview>), covering the period from January 1, 1984, to December 31, 20
664 24. Concurrently, the land use data were sourced from the Chinese Academy of Sciences
665 Resource and Environment Science Data Center (<https://www.resdc.cn/Default.aspx>). The co
666 re implementation of the VMD–Informer–LSTM model used in this study is publicly avail
667 able on GitHub at: <https://github.com/OUman648/vmd-informer-LSTM>.

669 Acknowledgements

670 This work was financially Supported by Open Research Fund Program of National Key
671 Laboratory of Water Disaster Prevention, 2024490711, Natural Science Foundation of Jiangsu
672 Province, BK20250906.

673 References

- 674 AghaKouchak, A., Farahmand, A., Melton, F. S., Teixeira, J., Anderson, M. C., Wardlow, B. D., &
675 Hain, C. R. (2015). Remote sensing of drought: Progress, challenges and opportunities.
676 *Reviews of Geophysics*, 53(2), 452–480. <https://doi.org/10.1002/2014RG000456>
- 677 Alsubih, M., Mallick, J., Talukdar, S., Salam, R., AlQadhi, S., Fattah, Md. A., & Thanh, N. V. (2021).
678 An investigation of the short-term meteorological drought variability over Asir Region of Saudi
679 Arabia. *Theoretical and Applied Climatology*, 145(1–2), 597–617.
680 <https://doi.org/10.1007/s00704-021-03647-4>
- 681 Belayneh, A., Adamowski, J., Khalil, B., & Ozga-Zielinski, B. (2014). Long-term SPI drought
682 forecasting in the Awash River Basin in Ethiopia using wavelet neural network and wavelet
683 support vector regression models. *Journal of Hydrology*, 508, 418–429.
684 <https://doi.org/10.1016/j.jhydrol.2013.10.052>
- 685 Bengio, Y., Courville, A., & Vincent, P. (2013). Representation Learning: A Review and New
686 Perspectives. *IEEE Transactions on Pattern Analysis and Machine Intelligence*, 35(8), 1798–
687 1828. <https://doi.org/10.1109/TPAMI.2013.50>
- 688 Box, G. E., Jenkins, G. M., Reinsel, G. C., & Ljung, G. M. (2015). *Time series analysis: Forecasting*
689 *and control*. John Wiley & Sons.
- 690 Cook, B. I., Mankin, J. S., Marvel, K., Williams, A. P., Smerdon, J. E., & Anchukaitis, K. J. (2020).
691 Twenty-First Century Drought Projections in the CMIP6 Forcing Scenarios. *Earth's Future*,
692 8(6), e2019EF001461. <https://doi.org/10.1029/2019EF001461>
- 693 Dai, A. (2013). Increasing drought under global warming in observations and models. *Nature*
694 *Climate Change*, 3(1), 52–58. <https://doi.org/10.1038/nclimate1633>
- 695 Dragomiretskiy, K., & Zosso, D. (2014). Variational Mode Decomposition. *IEEE Transactions on*
696 *Signal Processing*, 62(3), 531–544. <https://doi.org/10.1109/TSP.2013.2288675>
- 697 Dutra, E., Wetterhall, F., Di Giuseppe, F., Naumann, G., Barbosa, P., Vogt, J., Pozzi, W., &
698 Pappenberger, F. (2014). Global meteorological drought – Part 1: Probabilistic monitoring.
699 *Hydrology and Earth System Sciences*, 18(7), 2657–2667. <https://doi.org/10.5194/hess-18-2657-2014>
- 700
- 701 Ek, M. B., Mitchell, K. E., Lin, Y., Rogers, E., Grunmann, P., Koren, V., Gayno, G., & Tarpley, J.
702 D. (2003). Implementation of Noah land surface model advances in the National Centers for
703 Environmental Prediction operational mesoscale Eta model. *Journal of Geophysical Research*:

704 *Atmospheres*, 108(D22), 2002JD003296. <https://doi.org/10.1029/2002JD003296>

705 Gao, C., Zhang, Z., Zhai, J., Qing, L., & Mengting, Y. (2015). Research on meteorological
706 thresholds of drought and flood disaster: A case study in the Huai River Basin, China.
707 *Stochastic Environmental Research and Risk Assessment*, 29(1), 157–167.
708 <https://doi.org/10.1007/s00477-014-0951-y>

709 Greff, K., Srivastava, R. K., Koutník, J., Steunebrink, B. R., & Schmidhuber, J. (2017). LSTM: A
710 Search Space Odyssey. *IEEE Transactions on Neural Networks and Learning Systems*, 28(10),
711 2222–2232. <https://doi.org/10.1109/TNNLS.2016.2582924>

712 Hao, Z., Hao, F., Singh, V. P., Ouyang, W., & Cheng, H. (2017). An integrated package for drought
713 monitoring, prediction and analysis to aid drought modeling and assessment. *Environmental*
714 *Modelling & Software*, 91, 199–209. <https://doi.org/10.1016/j.envsoft.2017.02.008>

715 Hersbach, H., Bell, B., Berrisford, P., Hirahara, S., Horányi, A., Muñoz-Sabater, J., Nicolas, J.,
716 Peubey, C., Radu, R., Schepers, D., Simmons, A., Soci, C., Abdalla, S., Abellan, X., Balsamo,
717 G., Bechtold, P., Biavati, G., Bidlot, J., Bonavita, M., ... Thépaut, J. (2020). The ERA5 global
718 reanalysis. *Quarterly Journal of the Royal Meteorological Society*, 146(730), 1999–2049.
719 <https://doi.org/10.1002/qj.3803>

720 Hochreiter, S., & Schmidhuber, J. (1997). Long Short-Term Memory. *Neural Computation*, 9(8),
721 1735–1780. <https://doi.org/10.1162/neco.1997.9.8.1735>

722 Huang, S., Huang, Q., Chang, J., Zhu, Y., Leng, G., & Xing, L. (2015). Drought structure based on
723 a nonparametric multivariate standardized drought index across the Yellow River basin, China.
724 *Journal of Hydrology*, 530, 127–136. <https://doi.org/10.1016/j.jhydrol.2015.09.042>

725 Jacob, D., Petersen, J., Eggert, B., Alias, A., Christensen, O. B., Bouwer, L. M., Braun, A., Colette,
726 A., Déqué, M., Georgievski, G., Georgopoulou, E., Gobiet, A., Menut, L., Nikulin, G., Haensler,
727 A., Hempelmann, N., Jones, C., Keuler, K., Kovats, S., ... Yiou, P. (2014). EURO-CORDEX:
728 New high-resolution climate change projections for European impact research. *Regional*
729 *Environmental Change*, 14(2), 563–578. <https://doi.org/10.1007/s10113-013-0499-2>

730 Jaseena, K. U., & Koor, B. C. (2022). Deterministic weather forecasting models based on
731 intelligent predictors: A survey. *Journal of King Saud University - Computer and Information*
732 *Sciences*, 34(6, Part B), 3393–3412. <https://doi.org/10.1016/j.jksuci.2020.09.009>

733 Johny, K., Pai, M. L., & S., A. (2022). A multivariate EMD-LSTM model aided with Time
734 Dependent Intrinsic Cross-Correlation for monthly rainfall prediction. *Applied Soft Computing*,
735 123, 108941. <https://doi.org/10.1016/j.asoc.2022.108941>

736 Kratzert, F., Klotz, D., Brenner, C., Schulz, K., & Herrnegger, M. (2018). Rainfall–runoff modelling
737 using Long Short-Term Memory (LSTM) networks. *Hydrology and Earth System Sciences*,
738 22(11), 6005–6022. <https://doi.org/10.5194/hess-22-6005-2018>

739 Lawrence, D. M., Oleson, K. W., Flanner, M. G., Thornton, P. E., Swenson, S. C., Lawrence, P. J.,
740 Zeng, X., Yang, Z.-L., Levis, S., Sakaguchi, K., Bonan, G. B., & Slater, A. G. (2011).
741 Parameterization improvements and functional and structural advances in Version 4 of the
742 Community Land Model: PARAMETERIZATION IMPROVEMENTS AND FUNCTIONAL
743 AND STRUCTURAL ADVANCES. *Journal of Advances in Modeling Earth Systems*, 3(1),
744 n/a-n/a. <https://doi.org/10.1029/2011MS00045>

745 LeCun, Y., Bengio, Y., & Hinton, G. (2015). Deep learning. *Nature*, 521(7553), 436–444.
746 <https://doi.org/10.1038/nature14539>

747 Li, Z., Wu, H., Duan, S., Zhao, W., Ren, H., Liu, X., Leng, P., Tang, R., Ye, X., Zhu, J., Sun, Y., Si,

748 M., Liu, M., Li, J., Zhang, X., Shang, G., Tang, B., Yan, G., & Zhou, C. (2023). Satellite
749 Remote Sensing of Global Land Surface Temperature: Definition, Methods, Products, and
750 Applications. *Reviews of Geophysics*, 61(1), e2022RG000777.
751 <https://doi.org/10.1029/2022RG000777>

752 Lundberg, S., & Lee, S.-I. (2017). *A Unified Approach to Interpreting Model Predictions*
753 (arXiv:1705.07874; Version 2). arXiv. <https://doi.org/10.48550/arXiv.1705.07874>

754 Mishra, A. K., & Desai, V. R. (2005). Drought forecasting using stochastic models. *Stochastic*
755 *Environmental Research and Risk Assessment*, 19(5), 326–339.
756 <https://doi.org/10.1007/s00477-005-0238-4>

757 Mo, K. C. (2008). Model-Based Drought Indices over the United States. *Journal of*
758 *Hydrometeorology*, 9(6), 1212–1230. <https://doi.org/10.1175/2008JHM1002.1>

759 Modarres, R. (2007). Streamflow drought time series forecasting. *Stochastic Environmental*
760 *Research and Risk Assessment*, 21(3), 223–233. <https://doi.org/10.1007/s00477-006-0058-1>

761 Morid, S., Smakhtin, V., & Moghaddasi, M. (2006). Comparison of seven meteorological indices
762 for drought monitoring in Iran. *International Journal of Climatology*, 26(7), 971–985.
763 <https://doi.org/10.1002/joc.1264>

764 Mosavi, A., Ozturk, P., & Chau, K. (2018). Flood Prediction Using Machine Learning Models:
765 Literature Review. *Water*, 10(11), 1536. <https://doi.org/10.3390/w10111536>

766 Mossad, A., & Alazba, A. (2015). Drought Forecasting Using Stochastic Models in a Hyper-Arid
767 Climate. *Atmosphere*, 6(4), 410–430. <https://doi.org/10.3390/atmos6040410>

768 Muñoz-Sabater, J., Dutra, E., Agustí-Panareda, A., Albergel, C., Arduini, G., Balsamo, G., Boussetta,
769 S., Choulga, M., Harrigan, S., Hersbach, H., Martens, B., Miralles, D. G., Piles, M., Rodríguez-
770 Fernández, N. J., Zsoter, E., Buontempo, C., & Thépaut, J.-N. (2021). ERA5-Land: A state-of-
771 the-art global reanalysis dataset for land applications. *Earth System Science Data*, 13(9), 4349–
772 4383. <https://doi.org/10.5194/essd-13-4349-2021>

773 Myttenaere, A. D., Golden, B., Grand, B. L., & Rossi, F. (2016). Mean Absolute Percentage Error
774 for regression models. *Neurocomputing*, 192, 38–48.
775 <https://doi.org/10.1016/j.neucom.2015.12.114>

776 Nash, J. E., & Sutcliffe, J. V. (1970). River flow forecasting through conceptual models part I—A
777 discussion of principles. *Journal of Hydrology*, 10(3), 282–290.

778 Pozzi, W., Sheffield, J., Stefanski, R., Cripe, D., Pulwarty, R., Vogt, J. V., Heim, R. R., Brewer, M.
779 J., Svoboda, M., Westerhoff, R., Van Dijk, A. I. J. M., Lloyd-Hughes, B., Pappenberger, F.,
780 Werner, M., Dutra, E., Wetterhall, F., Wagner, W., Schubert, S., Mo, K., ... Lawford, R. (2013).
781 Toward Global Drought Early Warning Capability: Expanding International Cooperation for
782 the Development of a Framework for Monitoring and Forecasting. *Bulletin of the American*
783 *Meteorological Society*, 94(6), 776–785. <https://doi.org/10.1175/BAMS-D-11-00176.1>

784 Rummukainen, M. (2010). State-of-the-art with regional climate models. *WIREs Climate Change*,
785 1(1), 82–96. <https://doi.org/10.1002/wcc.8>

786 Saha, S., Moorthi, S., Wu, X., Wang, J., Nadiga, S., Tripp, P., Behringer, D., Hou, Y.-T., Chuang, H.,
787 Iredell, M., Ek, M., Meng, J., Yang, R., Mendez, M. P., Van Den Dool, H., Zhang, Q., Wang,
788 W., Chen, M., & Becker, E. (2014). The NCEP Climate Forecast System Version 2. *Journal of*
789 *Climate*, 27(6), 2185–2208. <https://doi.org/10.1175/JCLI-D-12-00823.1>

790 Schmidhuber, J. (2015). Deep learning in neural networks: An overview. *Neural Networks*, 61, 85–
791 117. <https://doi.org/10.1016/j.neunet.2014.09.003>

792 Shlezinger, N., Whang, J., Eldar, Y. C., & Dimakis, A. G. (2023). Model-Based Deep Learning.
793 *Proceedings of the IEEE*, 111(5), 465–499. <https://doi.org/10.1109/JPROC.2023.3247480>

794 Sit, M., Demiray, B. Z., Xiang, Z., Ewing, G. J., Sermet, Y., & Demir, I. (2020). A comprehensive
795 review of deep learning applications in hydrology and water resources. *Water Science and*
796 *Technology*, 82(12), 2635–2670. <https://doi.org/10.2166/wst.2020.369>

797 Svoboda, M., LeCompte, D., Hayes, M., Heim, R., Gleason, K., Angel, J., Rippey, B., Tinker, R.,
798 Palecki, M., Stooksbury, D., Miskus, D., & Stephens, S. (2002). THE DROUGHT MONITOR.
799 *Bulletin of the American Meteorological Society*, 83(8), 1181–1190.
800 <https://doi.org/10.1175/1520-0477-83.8.1181>

801 Trenberth, K. E., Dai, A., Van Der Schrier, G., Jones, P. D., Barichivich, J., Briffa, K. R., & Sheffield,
802 J. (2014). Global warming and changes in drought. *Nature Climate Change*, 4(1), 17–22.
803 <https://doi.org/10.1038/nclimate2067>

804 Vaswani, A., Shazeer, N., Parmar, N., Uszkoreit, J., Jones, L., Gomez, A. N., Kaiser, L., &
805 Polosukhin, I. (2017). Attention is all you need. *Advances in Neural Information Processing*
806 *Systems*, 30(1), 5998–6008.

807 Vicente-Serrano, S. M., Miralles, D. G., Domínguez-Castro, F., Azorin-Molina, C., El Kenawy, A.,
808 McVicar, T. R., Tomás-Burguera, M., Beguería, S., Maneta, M., & Peña-Gallardo, M. (2018).
809 Global Assessment of the Standardized Evapotranspiration Deficit Index (SEDI) for Drought
810 Analysis and Monitoring. *Journal of Climate*, 31(14), 5371–5393.
811 <https://doi.org/10.1175/JCLI-D-17-0775.1>

812 Wang, H., Liang, Q., Hancock, J. T., & Khoshgoftaar, T. M. (2024). Feature selection strategies: A
813 comparative analysis of SHAP-value and importance-based methods. *Journal of Big Data*,
814 11(1), 44. <https://doi.org/10.1186/s40537-024-00905-w>

815 Willmott, C., & Matsuura, K. (2005). Advantages of the mean absolute error (MAE) over the root
816 mean square error (RMSE) in assessing average model performance. *Climate Research*, 30,
817 79–82. <https://doi.org/10.3354/cr030079>

818 Wood, A. W., Hopson, T., Newman, A., Brekke, L., Arnold, J., & Clark, M. (2016). Quantifying
819 Streamflow Forecast Skill Elasticity to Initial Condition and Climate Prediction Skill. *Journal*
820 *of Hydrometeorology*, 17(2), 651–668. <https://doi.org/10.1175/JHM-D-14-0213.1>

821 Yao, T., Zhao, Q., Wu, C., Hu, X., Xia, C., Wang, X., Sang, G., Liu, J., & Wang, H. (2024). Spatio-
822 temporal Variation Characteristics of Extreme Climate Events and Their Teleconnections to
823 Large-scale Ocean-atmospheric Circulation Patterns in Huaihe River Basin, China During
824 1959–2019. *Chinese Geographical Science*, 34(1), 118–134. [https://doi.org/10.1007/s11769-](https://doi.org/10.1007/s11769-023-1398-1)
825 [023-1398-1](https://doi.org/10.1007/s11769-023-1398-1)

826 Yuan, S., & Quiring, S. M. (2017). Evaluation of soil moisture in CMIP5 simulations over the
827 contiguous United States using in situ and satellite observations. *Hydrology and Earth System*
828 *Sciences*, 21(4), 2203–2218. <https://doi.org/10.5194/hess-21-2203-2017>

829 Zhang, J., Xin, X., Shang, Y., Wang, Y., & Zhang, L. (2023). Nonstationary significant wave height
830 forecasting with a hybrid VMD-CNN model. *Ocean Engineering*, 285, 115338.
831 <https://doi.org/10.1016/j.oceaneng.2023.115338>

832 Zhang, L., Lin, J., Liu, B., Zhang, Z., Yan, X., & Wei, M. (2019). A Review on Deep Learning
833 Applications in Prognostics and Health Management. *IEEE Access*, 7, 162415–162438.
834 <https://doi.org/10.1109/ACCESS.2019.2950985>

835 Zhang, Q., Kong, D., Shi, P., Singh, V. P., & Sun, P. (2018). Vegetation phenology on the Qinghai-

836 Tibetan Plateau and its response to climate change (1982–2013). *Agricultural and Forest*
837 *Meteorology*, 248, 408–417. <https://doi.org/10.1016/j.agrformet.2017.10.026>

838 Zhang, Q., Zhang, J., Yan, D., & Wang, Y. (2014). Extreme precipitation events identified using
839 detrended fluctuation analysis (DFA) in Anhui, China. *Theoretical and Applied Climatology*,
840 117(1–2), 169–174. <https://doi.org/10.1007/s00704-013-0986-x>

841 Zhang, X., Duan, Y., Duan, J., Jian, D., & Ma, Z. (2022). A daily drought index based on
842 evapotranspiration and its application in regional drought analyses. *Science China Earth*
843 *Sciences*, 65(2), 317–336. <https://doi.org/10.1007/s11430-021-9822-y>

844 Zhao, L., Li, Z., Qu, L., Zhang, J., & Teng, B. (2023). A hybrid VMD-LSTM/GRU model to predict
845 non-stationary and irregular waves on the east coast of China. *Ocean Engineering*, 276, 114136.
846 <https://doi.org/10.1016/j.oceaneng.2023.114136>

847 Zhou, H., Zhang, S., Peng, J., Zhang, S., Li, J., Xiong, H., & Zhang, W. (2021a). Informer: Beyond
848 Efficient Transformer for Long Sequence Time-Series Forecasting. *Proceedings of the AAAI*
849 *Conference on Artificial Intelligence*, 35(12), 11106–11115.
850 <https://doi.org/10.1609/aaai.v35i12.17325>

851 Zhou, H., Zhang, S., Peng, J., Zhang, S., Li, J., Xiong, H., & Zhang, W. (2021b). Informer: Beyond
852 Efficient Transformer for Long Sequence Time-Series Forecasting. *Proceedings of the AAAI*
853 *Conference on Artificial Intelligence*, 35(12), 11106–11115.
854 <https://doi.org/10.1609/aaai.v35i12.17325>

855 Zuo, G., Luo, J., Wang, N., Lian, Y., & He, X. (2020). Decomposition ensemble model based on
856 variational mode decomposition and long short-term memory for streamflow forecasting.
857 *Journal of Hydrology*, 585, 124776. <https://doi.org/10.1016/j.jhydrol.2020.124776>

858